Received: 13 November 2019 | Revised: 25 December 2019 | Accepted: 2 January 2020

DOI: 10.1002/inf2.12086

REVIEW ARTICLE

WILEY

Low-dimensional metal halide perovskites and related optoelectronic applications

Pengchen Zhu | **Jia Zhu**

National Laboratory of Solid State Microstructures, Jiangsu Key Laboratory of Artificial Functional Materials, College of Engineering and Applied Sciences, Nanjing University, Nanjing, China

Correspondence
Jia Zhu, National Laboratory of Solid State Microstructures, Jiangsu Key Laboratory of Artificial Functional Materials, College of Engineering and Applied Sciences, Nanjing University, Nanjing 210 093, China.
Email: jiazhu@nju.edu.cn

Funding information
Fundamental Research Funds for the Central Universities, Grant/Award Numbers: 021314380135, 021314380128; Natural Science Foundation of Jiangsu Province, Grant/Award Number: BK20180341; National Natural Science Foundation of China, Grant/Award Numbers: 61735008, 11621091, 11874211, 11574143, 21805132

Abstract

Low-dimensional materials have pivotal significance in modern photonic, electronic, and optoelectronic areas due to their unique properties of the scale effect. Metal halide perovskites have revived in the optoelectronic fields recently, drawing intensive attention in photovoltaic devices, light-emitting diodes, lasers, photodetectors, and so on. Compared to their three-dimensional counterparts, the role of low-dimensional perovskites is becoming crucial, requiring a comprehensive understanding and exploration unceasingly. In this review, we examine low-dimensional perovskite of different forms and clarify various synthesis methods with morphological and dimensional control. Additionally, we also summarize potential optoelectronic applications based on their advantageous optical/electrical properties and enhanced mechanical integrity and stability. Finally, we propose a future perspective and possible developing directions in the exploration of novel perovskite-derived materials, new physics, and promising applications.

KEYWORDS

applications, low-dimension, metal halide perovskites, synthesis

1 | INTRODUCTION

Perovskite, which refers to specific compounds that possess a formula of ABX_3 (A and B sites are cations, and X site is anion) and the identical structure as $CaTiO_3$, has been investigated for more than a century.[1-7] In recent years, organic-inorganic metal halide perovskites, as one of the various types, have attracted much attraction due to their unique properties and remarkable device performances. In 2009, Kojima et al. utilized lead halide perovskite as sensitizers in dye-sensitized solar cells, achieving a solar-to-electricity power conversion efficiency (PCE) of 3.8%.[6] This research marks the new renaissance of metal halide perovskites first in PV devices. From that time on, the development of perovskite solar cells has dramatically ascended, achieving a certified PCE up to 25.2% (Best Research-Cell Efficiencies (NREL, 2019) https://www.nrel.gov/pv/assets/pdfs/best-research-cell-efficiencies.20190802.pdf). Due to the unique optoelectronic merits like high absorption coefficient, good defect-tolerant properties, ease of fabrication, and so on,[8-12] metal halide perovskites have extensive applications not only in PV field but also in other optoelectronic devices such as light-emitting diodes (LEDs), photodetectors, nanolasers, and so on.[13-21]

Bulk three-dimensional (3D) metal halide perovskites have a general structural formula of ABX_3, where A site

is a cation, typically the organic methylammonium (MA^+), formamidinium (FA^+) or inorganic cesium (Cs^+).[22-24] B site is metal, typically lead (Pb^{2+}), or tin cations (Sn^{2+}), and X site is the halide like chloride (Cl), bromide (Br), and iodide (I).[25-27] The term "3D" here focuses on the materials themselves and emphasizes the connected ways where $[BX_6]^{4-}$ octahedra consisting of one B cation, and six X anions are combined through corner sharing to form a 3D network. The A cation occupies the site in the middle of eight octahedra, and each element here needs to owe the proper valence state to keep a whole charge balance.[28-30]

To predict the 3D structure forming possibility, Goldschmidt tolerance factor (t) and octahedral factor (μ) are used as empirical rules. The definitions of t and μ are as following: $t = \frac{R_A + R_X}{\sqrt{2}(R_B + R_X)}$, $\mu = \frac{R_B}{R_X}$ where R_A, R_B, and R_X are the effective radii of the A, B, and X ions, respectively.[31,32] For a well-established 3D network, t and μ are usually in the range of 0.8-1.0 and 0.44-0.9, respectively.[10] Non-perovskite structures are often observed for improper-sized ions, for example, large A cations like $CH_3CH_2NH_3^+$ ($t > 1.0$) and small A cations like Rubidium ($t < 0.8$) will both lead to the collapse of the 3D structured network.[33-37] As observed empirically, distinguished advantages suitable for optoelectronics often vanish when switching to the non-perovskite structures.[38-40]

"Low-dimensional" perovskites refer to the perovskite compounds with at least one reduced dimension, in contrast to that with three unlimited extensions.[41-45] The term "low-dimensional" often leads to confusion due to its diverse meanings in different situations. In this review, we classify low-dimensional perovskites from two aspects: "material-level" and "structure-level" low dimensionalities.

The "material-level" low dimensionality emphasizes the perovskite material itself, underlining the building blocks of the perovskites that the individual components should have at least one dimension down to the molecular level. Specifically, these consisting parts made of $[BX_6]^{4-}$ octahedra usually exist in several forms, such as two-dimensional (layers), one-dimensional (wires), or separately zero-dimensional (polyhedrons) styles (Figure 1A). They are isolated by organic molecules and possess the dimension to one or several molecular units in one direction, at least. No matter they are assembled into nanostructures or even bulk films, the inherent properties remain nearly unchanged relative to the basic blocks.[44-50]

Differently, "structure-level" low-dimensional perovskites emphasize the final morphologies and commonly refer to those nanostructures of nanoplatelets/nanosheets, nanowires/nanorods, and nanocrystals (Figure 1B).[51-53] Mostly, these "structure-level" low-dimensional perovskites are made up of the 3D networks of corner-sharing

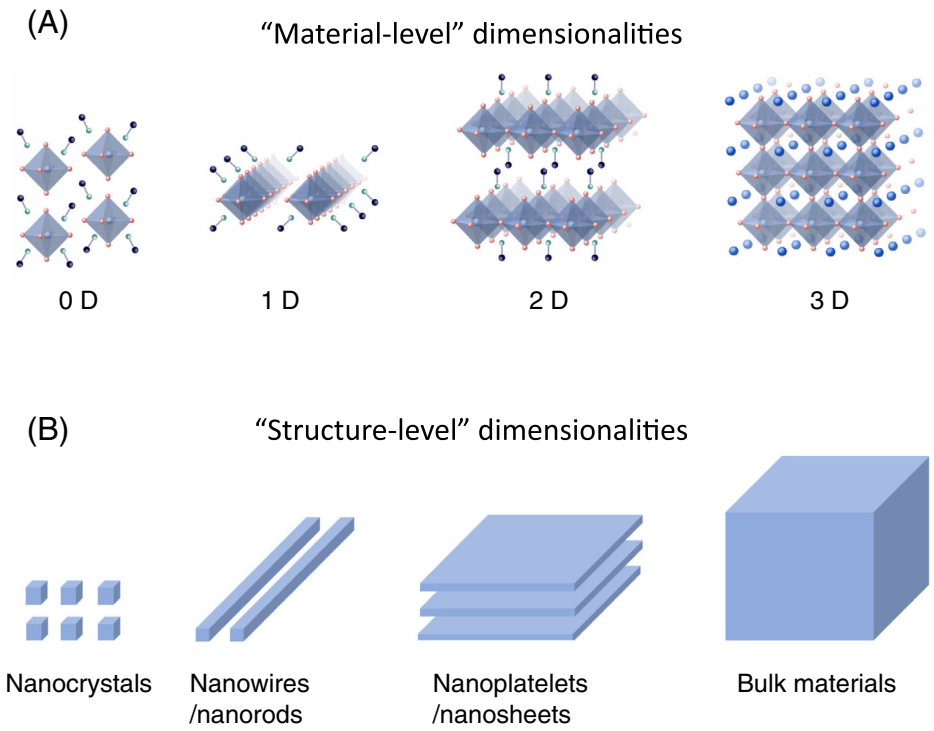

FIGURE 1 A, Schematic illustration of "material-level" low-dimensional perovskites and 3D perovskite. B, Schematic illustration of "structure-level" low-dimensional perovskites and perovskite bulk materials

$[BX_6]^{4-}$ octahedra, the same as that in bulk ABX_3 perovskites. In some specific cases, these nanostructures also consist of "material-level" low-dimensional individual species (layers, wires, or polyhedrons) as well.[54] From the above discussion, "structure-level" and "material-level" low dimensionalities are used to elaborate on different aspects and are not on opposite sides due to the partial overlap. In the following section, when referring to "structure-level" low-dimensional perovskites, we also use expressions such as nanoplatelets, nanowires, and nanocrystals to distinguish from "material-level" low-dimensional perovskites.

Compared to 3D counterparts commonly used, low-dimensional perovskites possess additional properties, mainly originating from their shape diversity and quantum confinement effects.[55-58] For example, due to the widely adjustable dimensions and sizes, low-dimensional materials usually own feasibly tunable bandgaps, enriching the wavelength range of absorption and emission.[59-61] Owing to the enlarged Coulombic force between electrons and holes, these electron-hole pairs have much higher binding energy and consequent high photoluminescent efficiency, which are desired for luminescent applications.[62-65] Also, strong anisotropic nature, together with enhanced surface-volume-ratio, could provide better contacts and smooth charge transport channel.[66,67] Finally, better crystallinity with reduced trap density and enlarged mechanical stability are often observed in low-dimensional material, greatly improving the optoelectronic device longevity and beneficial for flexible electronics.[68-71]

In this review, we will focus on the "structure-level" low-dimensional perovskites regardless of the consisting individuals (bulk, layers, wires, or polyhedrons). Meanwhile, some perovskite bulk forms consisting of "material-level" low-dimensional components are also selectively discussed in the following section.

2 | 2D METAL HALIDE PEROVSKITES

As the thickness reduces to several unit cells, the quantum confinement effect typically leads to larger binding energy, higher photoluminescence (PL), and increased bandgaps.[71] Perovskite nanosheets or nanoplatelets can be thought by minimizing the thickness of bulk 3D ABX_3 perovskite to a large extent. When they are extremely thin, the formula is no longer the ABX_3 but with a finite value of n: $A_{n+1}B_nX_{3n+1}$.[46] These thin nanosheets typically consist of similar networks as 3D counterparts, with two A cations terminated on the top and bottom sides.

In addition to these nanosheets, there is another "material-level" low type of two-dimensional (2D) perovskite, Ruddlesden-Popper (RP) phase perovskites, which have a chemical formula of $L_2A_{n-1}B_nX_{3n+1}$ (L is the long-chain cation and A is the smaller cation that can be fitted into the 3D lattice, like MA^+ or FA^+). The L normally has ammonium cations that can react with the terminated $[BX_6]^{4-}$ corner-shared layer and fit the periphery of these octahedra. These RP-type perovskites can be assembled into a bulk crystal or other nanostructures through the van der Waals interaction of each layer, keeping quantum confinement effects unchanged.[44,54,72-74] In this section, we concentrate on the synthesis methods and corresponding applications of nanoplatelets based on 3D networks and partially discuss the 2D RP-phase assembled bulk perovskites when referring to some optoelectronic applications.

2.1 | Synthesis methods

2.1.1 | All vapor-phase synthesis method

The bottom-up process is found to be feasible to achieve the desired 2D nanostructures. Considering the van der Waals layered nature of lead halides, it appears an effective way to acquire perovskite nanosheets with a start from PbX_2 nanoflakes (X = Cl/Br/I).[75-77] In 2014, Ha et al. developed a two-step method, combining chemical vapor deposition (CVD) and gas-solid reaction, to grow perovskite nanoplatelets (Figure 2A).[75] The authors first grew PbI_2 nanoplatelets on the muscovite mica substrates by van der Waals epitaxy in a vapor transport chemical deposition system. Then, they converted the as-formed PbI_2 nanoplatelets into perovskites by a gas-solid reaction with methylammonium iodide (MAI) molecular gas, slightly increasing the thickness after the incorporation of MAI molecular (Figure 2B).[75] The prepared perovskite nanoplatelets exhibit a lateral dimension of 5-30 μm and a thickness from dozens of to several hundreds of nanometers. By replacing the muscovite mica by SiO_2/Si substrates and altering the synthesis temperature and time, Niu et al. could precisely tune the thickness of perovskite nanoplatelets from few layers to several nanometers.[76] Besides, when employing rough-surfaced substrates, free-standing and large-scale PbI_2 nanosheets were synthesized by Lan et al. through the manipulation of microenvironment (Figure 2C).[77] Complete conversion to free-standing perovskite nanoflakes by CVD provides the promising potential for photon-detected applications.

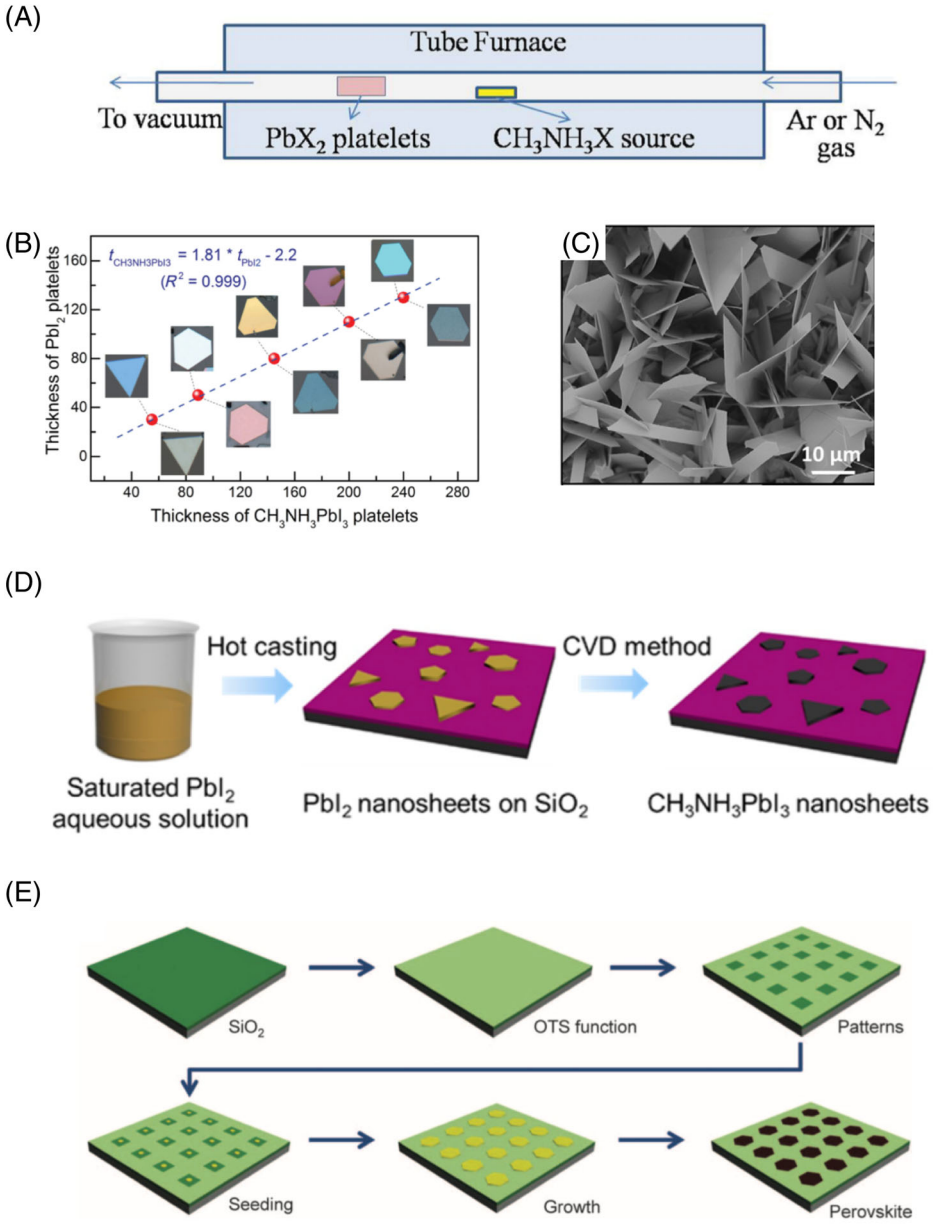

FIGURE 2 A, Schematic illustration of a two-step vapor-phase method for the synthesis of $MAPbX_3$ nanoplatelets (X = Cl/Br/I). B, The thickness correlation between PbI_2 nanoplatelets and converted $MAPbI_3$ nanoplatelets. Reproduced with permission.[75] Copyright 2014 Wiley-VCH. C, Scanning electron microscope (SEM) images of free-standing PbI_2 nanosheets from a vapor-phase synthesis method. Reproduced with permission.[77] Copyright 2017 Wiley-VCH. D, Schematic illustration of a combined solution- and vapor-phase synthesis method. Reproduced with permission.[78] Copyright 2016 American Chemical Society. E, Schematic illustration of the synthesis of perovskite micro-platelet arrays on pre-patterned substrates. Reproduced with permission.[79] Copyright 2015 AAAS

2.1.2 | Combined solution- and vapor-phase synthesis method

Thin PbI_2 nanoplatelets with the thickness down to monolayer can also be obtained by a facile solution process (Figure 2D).[78] Saturated PbI_2 aqueous solution was cast on a substrate, and 2D PbI_2 nanosheets would nucleate at an elevated temperature. Similar to the vapor-conversion process above, 2D $MAPbI_3$ perovskite nanosheets were formed by intercalating the MAI molecules into PbI_2 nanosheets under a gas atmosphere. Later, an impressive work by Wang et al. demonstrated well-patterned perovskite microplate arrays on a periodic substrate (Figure 2E).[79] Specifically, the substrates were partially treated with periodic hydrophilic patterns, where the PbI_2 seeds emerged after the seeding solution flew over.

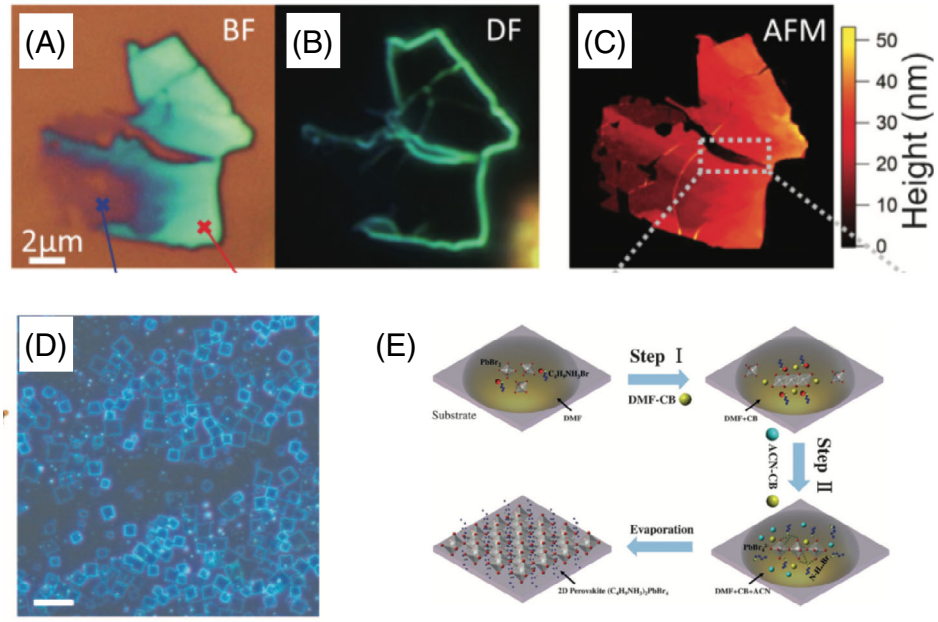

FIGURE 3 A-C, The microscopy (A-B) and AFM (C) images of RP perovskite $(C_6H_9C_2H_4NH_3)_2PbI_4$ nanosheets exfoliated from microcrystals. Reproduced with permission.[80] Copyright 2014 American Institute of Physics. D, Optical image of ultrathin BA_2PbBr_4 nanosheets synthesized from a direct solution growth method. Scale bar, 10 μm. Reproduced with permission.[83] Copyright 2015 AAAS. E, Different stages during the solution synthesis process of BA_2PbBr_4 nanosheets. Reproduced with permission.[84] Copyright 2017 Wiley-VCH

Afterward, a common vapor reaction process by MAI gas converted PbI_2 microplates into the desired perovskite plates. The successful realization of the periodic perovskite patterns proves the potential applications in integrated electronics.

2.1.3 | Exfoliation method

Different from the inherent ionic bond of nanoplatelets, the weak van der Waals interaction between neighboring layers makes it possible for RP type perovskite to be exfoliated into ultrathin nanosheets.[80-82] Niu et al. produced one to a few layers of thin flakes from $(C_6H_9C_2H_4NH_3)_2PbI_4$ crystals (Figure 3A-C).[80] Hexagonal RP type $(C_6H_9C_2H_4NH_3)_2PbI_4$ perovskite microcrystals with 30 μm lateral size were first synthesized, followed by a micromechanical exfoliation technique to create ultrathin flakes. This method is rather suitable for the investigation of fundamental properties but inconvenient for high production due to the uncontrollable size and thickness.

2.1.4 | Direct solution growth method

In 2015, Dou et al. proposed a direct solution growth method to synthesize atomically thin RP type BA_2PbI_4 ($BA = C_4H_9NH_3^+$) perovskite nanosheets. A much diluted precursor in ternary organic solvents was cast on flat substrates, where acetonitrile (ACN) and chlorobenzene were used to reduce the solubility of BA_2PbI_4 in dimethylformamide (DMF) and promote the crystallization (Figure 3D).[83] Thus, a single-unit layer, with a thickness of ~1.6 nm, was successfully demonstrated. Based on this work, Chen et al. further studied the critical factors systematically, including crystallization temperature, solvent ratio, and polarity on the growth dynamics (Figure 3E).[84] They assumed that the formation of large-size thin sheets was governed by the effects of diffusion-mechanism-dominated branched growth, together with CAN-induced c-axis suppression. Under the optimized condition, 2D BA_2PbBr_4 perovskites with the lateral sizes up to 40 μm and thicknesses down to a few nanometers were obtained. These works above suggest that the solution growth method can be suitable to achieve high-quality perovskite nanosheets with controllable thickness.

2.1.5 | Colloidal growth method

Due to the great success in the synthesis of inorganic quantum dots like CdSe and ZnSe,[85-88] the colloidal growth method has vital importance in the perovskite nanostructure fabrication.[60,89] In 2015, Tyagi et al. adapted a precipitation method used for perovskite nanoplatelet

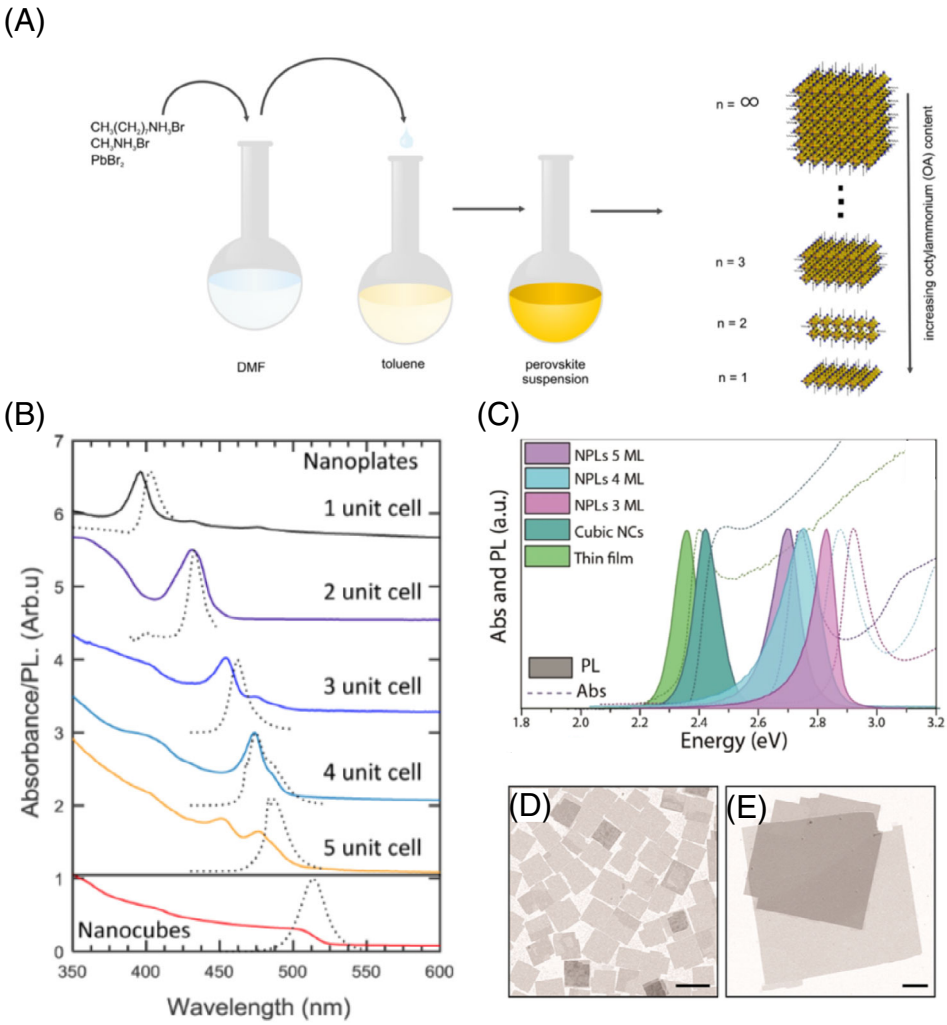

FIGURE 4 A, Schematic illustration of the synthesis of the perovskite nanoplatelets by a colloidal synthesis method. The thickness was controlled by the ratio of OABr in the precursor. Reproduced with permission.[60] Copyright 2015 American Chemical Society. B, Absorption (solid lines) and emission (dashed lines) spectra of $CsPbBr_3$ nanotubes and nanoplatelets with different thicknesses. Reproduced with permission.[90] Copyright 2015 American Chemical Society. C, Absorption and PL spectra of $CsPbBr_3$ thin film, cube-shaped nanocrystals, and nanoplatelets with different thicknesses from a room-temperature synthesis scheme. Reproduced with permission.[91] Copyright 2016 American Chemical Society. D-E, Transmission electron microscope (TEM) images of $CsPbBr_3$ nanoplatelets with different lateral sizes. The scale bars are 1 μm. Reproduced with permission.[92] Copyright 2016 American Chemical Society

synthesis, where octylammonium bromide (OABr) was chosen as the long-chain ligands.[89] Later, Sichert et al. synthesized $MAPbBr_3$ nanoplatelets by a modified process where they added a mixed solution of $PbBr_2$, OABr, and MABr in DMF into toluene dropwise (Figure 4A).[60] The thicknesses of these nanoplatelets were well controlled from one to several units by varying the adding amount of OABr. Bekenstein et al. reported the colloidal synthesis of highly luminescent (photoluminescent quantum yield [PLQY] 84%) inorganic $CsPbX_3$ nanoplatelets with the thickness of 1-5 unit cells, showing adjustable PL emissions due to strong quantum size effect (Figure 4B).[90] A facile anion exchange process further promoted the PL emissions covering the entire visible spectrum. The systematic investigations facilitated the following development of the $CsPbX_3$ nanoplatelet synthesis, with a more precise thickness control (Figure 4C) and an enlarged lateral size up to micrometer range (Figure 4D-E).[91,92]

2.2 | Applications of 2D metal halide perovskites

Solar cells employing 3D perovskites have achieved considerable improvements in the past few years, yielding a certified PCE up to 25.2%.[7] Along with the rapid PCE development, the instability problem has been proposed

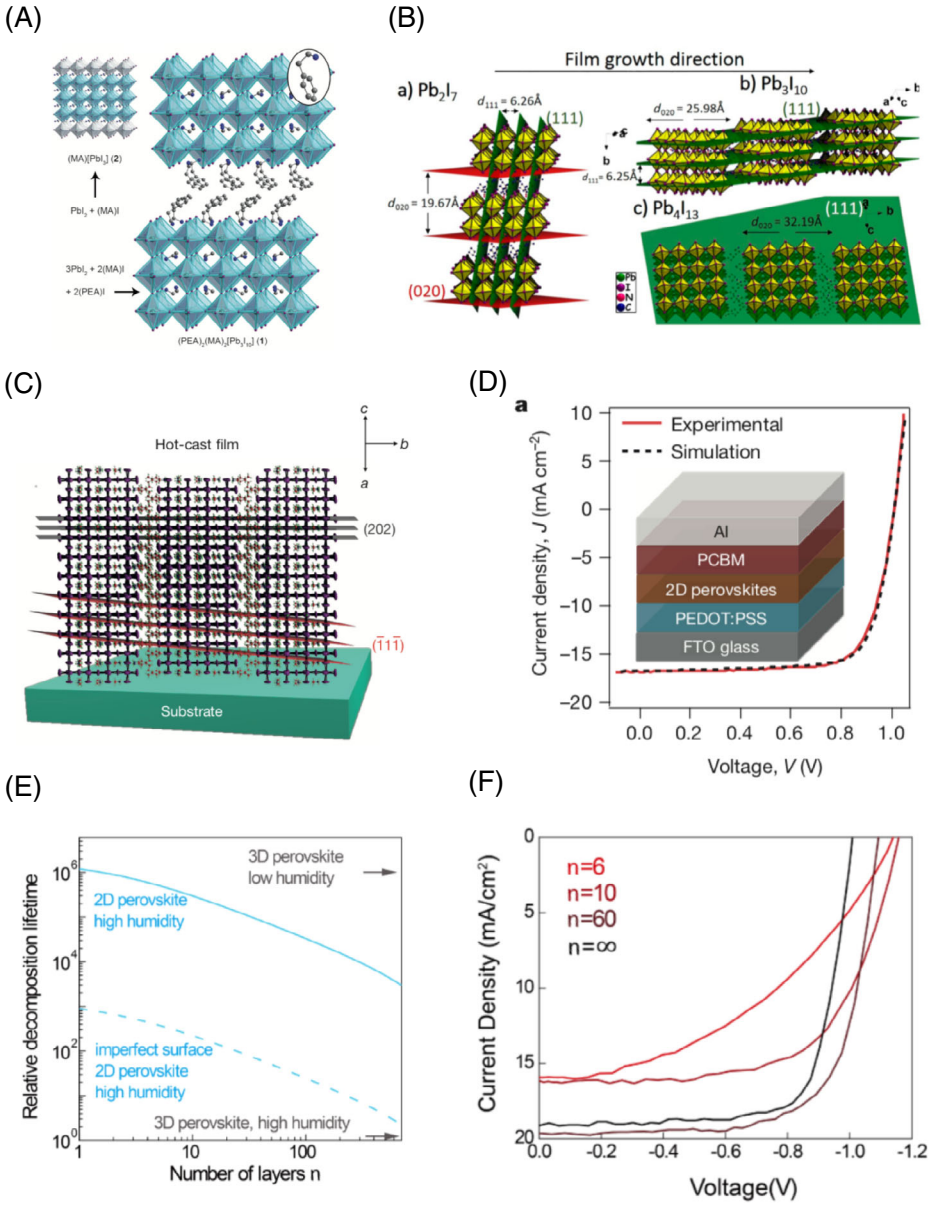

FIGURE 5 A, Crystal structures of the three-dimensional (3D) perovskite $MAPbI_3$ and the two-dimensional (2D) Ruddlesden-Popper (RP) perovskite $(PEA)_2(MA)_2Pb_3I_{10}$. Atom colors: Pb = turquoise, I = purple, N = blue, and C = gray. Disordered atoms and hydrogen are omitted for clarity. Reproduced with permission.[93] Copyright 2014 Wiley-VCH. B, Schematic of film growth orientations of 2D $(BA)_2(MA)_{n-1}Pb_nI_{3n+1}$ with different n values (n = 2, 3, and 4). Reproduced with permission.[94] Copyright 2015 American Chemical Society. C, Schematic of the (101) orientation, along with the (111) and (202) planes of a 2D perovskite crystal from the hot-casting method. D, Experimental and simulated current-density-voltage (J-V) curves under AM.1.5G solar illumination by using 2D $(BA)_2(MA)_3Pb_4I_{13}$ perovskites as the absorbing layer at an optimized thickness (230 nm). The inset is the device structure. Reproduced with permission.[98] Copyright 2016 Nature Publishing Group. E, Density functional theory (DFT) simulation of the formation energy of perovskite with different n values in different atmospheres. F, Experimental J-V curves of perovskite solar cells employing 2D $(PEA)_2(MA)_{n-1}Pb_nI_{3n+1}$ with different n values. Reproduced with permission.[99] Copyright 2016 American Chemical Society

as a considerable issue. Compared to the traditional 3D ABX_3 perovskite, 2D RP layered perovskite has a much more enhanced moisture tolerance and can improve the stability to a certain extent.[93-95] In addition to this benefit, the confinement in 2D perovskite will bring up large binding energy and improve the photoluminescent efficiency, which is promising for the application of emissions like LEDs and lasers.[96,97] In the following section, we will discuss the optoelectronic applications based on 2D perovskites, including not only nanosheets or nanoplatelets but also some unique forms of RP type perovskites.

TABLE 1 Summary of key parameters of solar cells based on low-dimensional perovskites

Materials	Structures	Device configuration	V_{oc} (V)	J_{sc} (mA cm^{-2})	FF (%)	PCE (%)	References
$PEA_2MA_2Pb_3I_{10}$	Thin film	FTO/c-TiO_2/PVSK/spiro-OMeTAD/Au	1.18	6.72	60.0	4.73	93
$PEA_2MA_4Pb_5I_{16}$	Thin film	ITO/PEDOT:PSS/PVSK/PCBM/BCP/Ag	1.19	15.8	75.0	14.1	100
$PEA_2MA_4Pb_5I_{16}$	Thin film	FTO/c-TiO_2/PVSK/spiro-OMeTAD/Au	1.12	16.42	67.0	12.29	101
$(iso\text{-}BA)_2MA_3Pb_4I_{13}$	Thin film	FTO/C_{60}/PVSK/spiro-OMeTAD/Au	1.20	16.54	53.54	10.63	102
$(3BBA)_2MA_{n-1}Pb_nI_{3n+1}$ $(3 < n < 4)$	Thin film	ITO/PTAA/PVSK/PCBM/Cr/Au	1.23	18.22	81.2	18.2	103
$BA_2MA_2Pb_3I_{10}$	Thin film	FTO/c-TiO_2/m-TiO_2/PVSK/spiro-OMeTAD/Au	0.929	9.42	46.0	4.02	94
$BA_2MA_3Pb_4I_{13}$	Thin film	FTO/PEDOT:PSS/PVSK/PCBM/Al	1.01	16.76	74.13	12.51	98
$BA_2MA_2Pb_3I_{10}$	Thin film	ITO/PEDOT:PSS/PVSK/PCBM/BCP/Ag	0.97	12.79	55.0	6.82	104
$BA_2MA_3Pb_4I_{13}$	Thin film	ITO/PEDOT:PSS/PVSK/PCBM/BCP/Ag	0.98	14.71	61.0	8.79	104
$BA_2MA_3Pb_4I_{13}$	Thin film	ITO/PEDOT:PSS/PVSK/PCBM/PEIE/Ag	1.14	18.8	69.5	14.9	105
$BA_2MA_3Pb_4I_{13}$	Thin film	ITO/PTAA/PVSK/C_{60}/BCP/Ag	1.24	19.86	70.44	17.26	106
$BA_2MA_4Pb_5I_{16}$	Thin film	ITO/PEDOT:PSS/PVSK/PCBM/Al	0.986	15.5	65.5	10.0	107
$BA_2(MA_{0.8}FA_{0.2})_3Pb_4I_{13}$	Thin film	ITO/PEDOT:PSS/PVSK/PCBM/BCP/Ag	0.999	18.12	70.79	12.81	108
$BA_2(Cs_{0.05}MA_{0.95})_3Pb_4I_{13}$	Thin film	FTO/c-TiO_2/PVSK/spiro-OMeTAD/Au	1.08	19.95	63.47	13.68	109
$[(BA)_{0.94}(F_3EA)_{0.06}]_2MA_3Pb_4I_{13}$	Thin film	ITO/PEDOT:PSS/PVSK/PCBM/BCP/Ag	1.02	16.08	76.3	12.51	110
$FA_xPEA_{1-x}PbI_3$ (FAI/PEAI = 40)	Thin film	ITO/NiO_x/PVSK/PCBM/bis-C_{60}/Ag	1.04	22.08	77.13	17.71	111
$PEA_2MA_{n-1}Pb_nI_{3n+1}$ (n = 60)	Thin film	FTO/c-TiO_2/PVSK/spiro-OMeTAD/Au	1.09	19.12	73.70	15.36	99
$PEA_2MA_{n-1}Pb_nI_{3n+1}$ (PEAI/PbI_2 = 0.05)	Thin Film	FTO/c-TiO_2/m-TiO_2/PVSK/spiro-OMeTAD/Ag	1.08	21.91	80.36	19.10	112
$BA_{0.09}(FA_{0.83}Cs_{0.17})_{0.91}Pb(I_{0.6}Br_{0.4})_3$	Thin film	FTO/SnO_2/PCBM/PVSK/spiro-OMeTAD/Au	1.18	19.8	73.0	17.2	113
$BA_{0.05}(FA_{0.83}Cs_{0.17})_{0.91}Pb(I_{0.8}Br_{0.2})_3$	Thin film	FTO/SnO_2/PCBM/PVSK/spiro-OMeTAD/Au	1.14	22.7	80.0	20.6	113
$(EDBEPbI_4)_{0.03}[Cs_{0.05}(FA_{0.83}Cs_{0.17})_{0.95}Pb(I_{0.83}Br_{0.17})_3]_{0.97}$	Thin film	FTO/SnO_2/PVSK/spiro-OMeTAD/Au	1.13	23.53	79.2	21.06	114
$ThMA_2MA_{n-1}Pb_nI_{3n+1}$	Thin film	ITO/SnO_2/PVSK/spiro-OMeTAD/MoO_3/Ag	1.16	22.88	81.0	21.49	115
$MAPbI_3$	Nanowires	FTO/c-TiO_2/m-TiO_2/PVSK/spiro-OMeTAD/Au	1.052	19.12	72.1	14.71	116
$MAPbI_3$	Nanowires	ITO/PEDOT:PSS/PVSK/P(NDI2OD-T2)/PEI/Ag/Al_2O_3	1.01	23.39	79.74	18.83	117

(Continues)

TABLE 1 (Continued)

Materials	Structures	Device configuration	V_{oc} (V)	J_{sc} (mA cm^{-2})	FF (%)	PCE (%)	References
$MAPbI_3$	Nanowires	FTO/c-TiO_2/PVSK/ spiro-OMeTAD/Au	1.04	23.8	74.6	18.42	118
$MAPbI_3$	Nanowires	FTO/c-TiO_2/PVSK/ spiro-OMeTAD/Au	1.12	22.47	70	17.62	119
$CsPbBr_3$	Nanowires	FTO/c-TiO_2/PVSK/ spiro-OMeTAD/Au	0.851	2.96	44.5	1.21	120
$CsSnI_3$	Nanocrystals	ITO/c-TiO_2/PVSK/ spiro-OMeTAD/Au	0.86	23.2	0.65	12.96	121
$MAPbBr_3$	Nanocrystals	FTO/c-TiO_2/m-TiO_2/PVSK/ PTAA/Au	1.110	14.07	73.0	11.40	122
$FAPbI_3$	Nanocrystals	ITO/SnO_2/PVSK/spiro-OMeTAD/ Au	1.10	11.83	64.42	8.38	123
$FAPbI_3$	Nanocrystals	ITO/SnO_2/PVSK/spiro-OMeTAD/ Ag	1.10	15.4	74.8	12.7	124
$CsPbI_3$	Nanocrystals	FTO/c-TiO_2/PVSK/ spiro-OMeTAD/MoO_x/Al	1.23	13.47	65.0	10.77	125
$CsPbI_3$	Nanocrystals	FTO/c-TiO_2/PVSK/ spiro-OMeTAD/MoO_x/Al	1.20	14.37	78.0	13.4	126
$CsPbI_3$	Nanocrystals	FTO/c-TiO_2/μ-GR/PVSK/PTAA/ Au	1.18	13.59	72.6	11.40	127
$CsPbI_3$	Nanocrystals	FTO/c-TiO_2/PVSK/PTB7/MoO_3/ Ag	1.27	12.39	80.0	12.55	128
$Cs_{0.25}FA_{0.75}PbI_3$: $CsPbI_3$	Nanocrystals	ITO/c-TiO_2/PVSK/ spiro-OMeTAD/MoO_x/Al	1.20	18.91	76.0	17.39	129
$CsPbI_3$: $FAPbI_3$	Nanocrystals	FTO/c-TiO_2/PVSK/PTAA/MoO_3/ Ag	1.22	17.26	74.0	15.6	130

Note: J_{sc}, short-circuit current; V_{oc}, open-circuit voltage; FF, fill factor; PCE, power conversion efficiency.

2.2.1 | Solar cells

The first generation of solar cells utilizing an RP type perovskite $PEA_2MA_2Pb_3I_{10}$ (PEA = $C_6H_5[CH_2]_2NH_3^+$) as the absorber was fabricated by Smith et al. (Figure 5A) exhibiting a PCE of 4.73%.[93] Although this efficiency falls behind that based on 3D perovskites, the moisture tolerance, which is essential for large-scale manufacture and broad commercialization, shows much superior performance than its bulk counterpart.[93] Later, Cao et al. reported another RP type perovskite-based solar cell by using a relatively shorter organic cations BA (Figure 5B). Due to the self-assembly nature, the 2D compounds with $n > 2$ values ($BA_2MA_{n-1}Pb_nI_{3n+1}$) were formed with preferential growth orientation, beneficial for charge transport and formation of smooth thin films.[94] Interestingly, when adopting a planar structure, the photovoltaic (PV) parameters were much poorer compared to the mesoporous structure, attributed to the short diffusion length of photocarriers in the 2D RP type perovskite.[94] Tsai et al. proposed a similar hypothesis that insufficient charge transport could lead to worse performance arose from the nonideal layer orientation, where organic cations acted like insulating spacing layers between the conducting inorganic slabs. By applying a proposed hot-casting method here (Figure 5C), they produced $BA_2MA_{n-1}Pb_nI_{3n+1}$ thin films of near-single-crystalline quality, where the crystallographic planes of the inorganic perovskite had a preferential orientation perpendicular to both contacts.[98] In a planar structure employing $BA_2MA_3Pb_4I_{13}$ as absorber, they obtained a PCE of 12.52%, among the highest efficiency of low-dimensional perovskite solar cells at that time (Figure 5D). Unencapsulated and encapsulated devices both exhibited much-enhanced stability when exposed to humidity and constant illumination. As the layer number n can effectively affect the device performance and stability, a systematical exploration to understand this

correlation and inherent mechanism is in a request. Quan et al. fabricated quasi-2D perovskite films that exhibited enhanced stability without sacrificing the high performance of 3D $MAPbI_3$ perovskites (Figure 5F).[99] Confirmed by density functional theory, the instability issue of 3D perovskites originates from the low formation energy and becomes aggravated when taking high humidity into account (Figure 5E). The addition of larger organic cation to form quasi-2D perovskite could enlarge the formation energy owing to the appreciable van der Waals forces that conferred enhanced stability. This work provides one possible elucidation of why 2D or quasi-2D perovskites own improved stability, especially when exposed to high moisture. For clear comparison, we summarize the key parameters of solar cells based on 2D perovskites in Table 1.

2.2.2 | Light-emitting diodes

Enlarged binding energy and strong PLQY from quantum confinement make 2D perovskites suitable for the applications of LEDs.[131-133] The first 2D RP perovskite-based LEDs can date back to the mid-1990s, where Era et al. demonstrated the device by incorporating a layered perovskite compound PEA_2PbI_4, showing an emission peak at 520 at liquid-nitrogen temperature.[131] However, when driven at room temperature, the electroluminescence (EL) efficiency became rather low, which could be explained by the thermal quenching of photoluminescent in the perovskite film. Thus, fabricating efficient LEDs with certain EL efficiency at room temperature is a demanding trend. Liang et al. improved the crystal quality by converting poly-crystalline PEA_2PbBr_4 thin films into single-crystalline micro-sized nanoplates via solvent vapor annealing and showed efficient room-temperature violet EL at 410 nm (Figure 6A).[132] Compared to the pure phase RP perovskite components (one value of n only), poly-crystalline RP perovskite films containing multiple phases (multiple values of n) have superior light-emission performance.[134-137,139-141] Yuan et al. and Huang et al. independently reported LEDs incorporated with mixed layered perovskite materials, displaying impressive performance and stability. The mixed compounds act like a photocarrier concentrator, funneling the charge carriers from high-bandgap materials to the lowest-bandgap ones and boosting the external quantum efficiency (EQE) to 8.8% and 11.7% (Figure 6B-C), respectively.[134,135] Jiang et al. tuned the "A-site" cation by using a Rubidium-Cesium alloyed perovskite, demonstrating a spectra-stable blue LED with a peak EQE of 1.35% (Figure 6D).[136] In addition to the composition engineering, other strategies like surface passivation, crystallite tailoring, structure engineering, and so forth were also applied for performance and longevity improvement.[137-141] Yang et al. utilized trioctylphosphine oxide treatment to passivate the surface of quasi-2D $PEA_2(FAPbBr_3)_{n-1}PbBr_4$ films, achieving an EQE of 14.36%.[140] Xiao et al. added large-group ammonium as a surfactant to constrain the growth of 3D grains, producing smooth films consisting of crystallites with a size of about 10 nm.[141] Through the incorporation of small ions such as sodium (Na^+) to substitute the large organic molecules, Wu et al. overcame the charge transport issue resulting from the insulating long-chain cation and achieved a high EQE of 15.9% (Figure 6E,F).[137] To further boost the EL efficiency of LEDs, Zhao et al. demonstrated a perovskite-polymer bulk heterostructure (PPBH) to suppress non-radiative recombination channels and obtained an EQE up to 20.1% (Figure 6G).[138] Bipolar host materials like PVK: PBD were also incorporated for the protection, enabling glove-box free fabrication of LEDs, with efficient green photoluminescence and long-term stability.[142] Detailed key parameters of 2D perovskite-based LEDs are summarized in Table 2.

2.2.3 | Photodetectors

Owing to the large absorption coefficient, high carrier mobility, and good compatibility with flexible substrates, perovskite nanosheets are also appropriate for photodetectors.[77,159-161] In 2015, Liu et al. demonstrated a thin $MAPbI_3$ nanosheet-based photodetector through a combined solution process and vapor-phase conversion method (Figure 7A).[78] Under the incidence at 405 and 532 nm, the current density was significantly increased, showing photo responsivities of 22 and 12 AW^{-1} (at 1 V) and fast response time (Figure 7B,C). Wang et al. grew 2D perovskite microcrystals on patterned electrodes (Figure 7D), creating independently addressable photodetector arrays and functional field-effect transistors (Figure 7E,F).[79] In addition, photodetector based on inorganic perovskite nanosheets (like $CsPbX_3$, X = I/Br/Cl) has analogous performances compared to their organic counterparts.[161-163] Due to the ultra-smooth surface and high optical response, a flexible detector based on monolayer and few-layer $CsPbBr_3$ nanosheets showed superior electrical stability even after 10 000 times of bending (Figure 7G,H).[161] The following optimization to increase carrier extraction and transport by a combination of CNTs and $CsPbBr_3$ nanosheets (Figure 7I) enabled a flexible photodetector with an EQE and responsivity as high as 7488% and 31.1 AW^{-1} (Figure 7J).[162] A summary of the key parameters of photodetectors based on 2D perovskites is exhibited in Table 3.

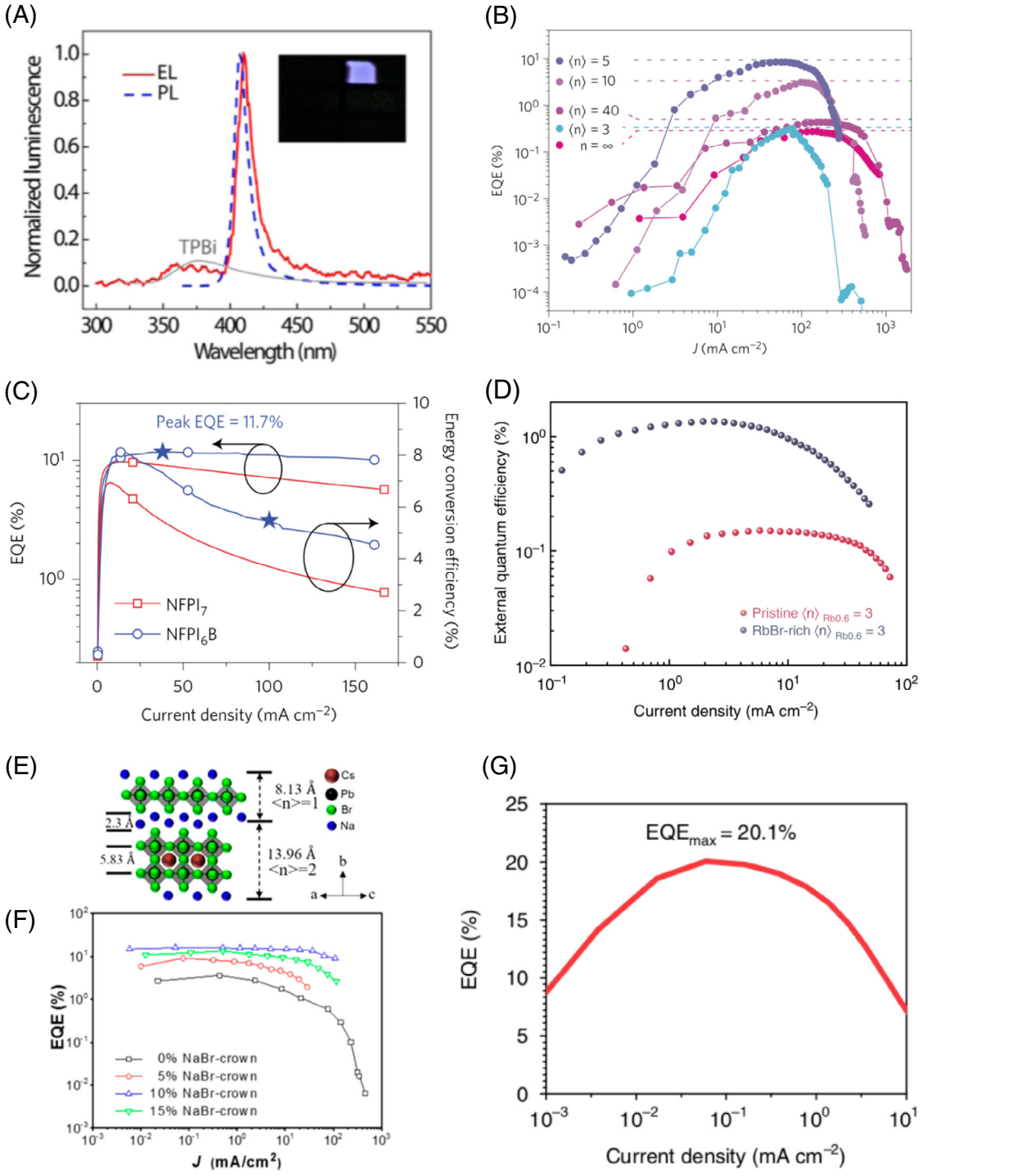

FIGURE 6 A, Normalized photoluminescence (PL) and electroluminescence (EL) (at 6 V) spectra of an light-emitting diode (LED) device based on the $(PEA)_2PbBr_4$ nanoplatelets. Reproduced with permission.[132] Copyright 2016 American Chemical Society. B, External quantum efficiency (EQE) values of two-dimensional (2D) Ruddlesden-Popper (RP) perovskite-based LEDs vs current density. Reproduced with permission.[134] Copyright 2016 Nature Publishing Group. C, EQE and energy conversion efficiency vs current density for the $NFPI_7$ and $NFPI_6B$-based LED. Reproduced with permission.[135] Copyright 2016 Nature Publishing Group. D, EQE values of 2D RP perovskite-based LEDs vs current density. Reproduced with permission.[136] Copyright 2019 Nature Publishing Group. E, View of the unit cell of $Na_2Cs_{n-1}Pb_nBr_{3n+1}$ perovskites with different values of ⟨n⟩ (1 and 2). F, EQE-J values of devices based on 2D-3D perovskite films with different NaBr molar ratios. Reproduced with permission.[137] Copyright 2019 American Chemical Society. G, EQE-current density characteristics of the best perovskite-polymer bulk heterostructure (PPBH) LED. Reproduced with permission.[138] Copyright 2018 Nature Publishing Group

TABLE 2 Summary of key parameters of LEDs based on low-dimensional perovskites

Materials	Structures	EL λ_{max} (nm)	Max EQE (%)	Max CE (cd A^{-1})	Max PE (lm W^{-1})	Max L (cd m^{-2})	References
$PEA_2MA_4Pb_5I_{16}$	Thin film	~760	8.8	N/A	N/A	N/A	134
NMAI:FABr:PbI_2 = 2:1:2	Thin film	763	11.7	N/A	N/A	N/A	135
$PEA_2(FAPbBr_3)_2PbBr_4$	Thin film	532	14.36	62.43	53.3	9120	140
$PEA_2(Rb_xCs_{1-x})_2Pb_3Br_{10}$	Thin film	475	1.35	N/A	N/A	100.6	136
$BA_2MA_3Pb_4I_{13}$	Thin film	733	0.2	N/A	N/A	N/A	143
$BA_2MA_4Pb_5I_{16}$	Thin film	744	0.5	N/A	N/A	N/A	143
$PEA_2(FAPbBr_3)_2PbBr_4$	Thin film	532	15.4	67.5	N/A	15 765	144
$Na_2Cs_{n-1}Pb_nBr_{3n+1}$	Thin film	518	15.9	50.3	45.1	11 560	137
BAI:$MAPbI_3$ = 1:5	Thin film	748	10.4	0.09	0.10	N/A	141
BABr:$MAPbBr_3$ = 1:5	Thin film	513	9.3	17.1	13.0	N/A	141
$BA_2Cs_{n-1}Pb_nI_{3n+1}$	Thin film	680	6.23	1.74	1.37	1392	145
$NMA_2FA_{n-1}Pb_nI_{3n+1}$	Thin film	795	20.1	N/A	N/A	N/A	138
$NMA_2(CsPbI_3)_{n-1}PbI_4(Cl)$	Thin film	688	3.7	N/A	0.24	440	146
$PEA_2Cs_{n-1}Pb_n(Cl_xBr_{1-x})_{3n+1}$	Thin film	480	5.7	6.1	N/A	3780	147
$MAPbBr_3$	Nanoplatelets	530	0.48	N/A	1.0	10 590	142
$PEAPbBr_4$	Nanoplatelets	410	0.31	0.19	0.10	147.6	148
$PEAPbBr_4$	Nanoplatelets	410	0.038	N/A	N/A	N/A	132
$MAPbBr_3$	Nanorods	533	N/A	N/A	N/A	N/A	149
$MAPbBr_3$	Nanocrystals	532	N/A	9.2	N/A	3187	150
$FA_{0.8}Cs_{0.2}PbBr_3$	Nanocrystals	~525	2.8	10.09	N/A	55 005	151
$CsPbBr_3$	Nanocrystals	516	0.12	0.43	0.18	946	152
$CsPbBr_3$	Nanocrystals	512	6.72	13.3	5.24	15 185	153
$CsPbBr_3$	Nanocrystals	515	3.0	N/A	N/A	330	154
$CsPbBr_3$	Nanocrystals	510	0.325	N/A	N/A	934	155
$CsPbBr_3$	Nanocrystals	518	16.48	66.7	65.9	76 940	156
$CsPbBr_xI_{1-x}$	Nanocrystals	653	21.3	10.6	11.9	500	157
$CsPbI_3$	Nanocrystals	698	5.7	N/A	N/A	206	158

Note: EL, electroluminescence; CE, current efficiency; PE, power efficiency; L, luminance; EQE, external quantum efficiency.

2.2.4 | Lasers

It is well known that well-faceted nanowires with suitable diameters support predominantly axial Fabry-Pérot waveguide modes in nanolasers.[174] Apart from this, whispering-gallery mode existing in micro/nanodisks can utilize successive total internal reflection along the circumference and provide high cavity quality factor.[175-178] In 2014, Zhang et al. realized room-temperature near-infrared nanoplatelet lasers using $MAPbI_{3-a}X_a$ (X = I,Br, Cl) nanoplatelets (Figure 8A).[176] This wavelength-tunable nanolaser (Figure 8B) could be easily integrated onto conductive platforms like Si, Au, and indium tin oxide, promising for the integrity of existing Si technology. Later, the same group fabricated all inorganic nanoplatelet lasers, where the whispering-gallery mode cavities showed multicolor lasing (Figure 8C) with a low threshold (~2 μJ cm^{-2}) and high spectra coherence (~0.14-0.15 nm).[179] 2D RP type perovskites widely integrated in LEDs are also desirable for the application of lasers for its high PL efficiency. Zhang et al. demonstrated a novel microring laser array based on the $(BA)_2(MA)_{n-1}Pb_nBr_{3n+1}$ perovskites (Figure 8D).[180] For a given value of n, the practically mixed composition render photocarriers to transfer from the high-bandgap perovskites to the lowest-bandgap ones, enabling the

population inversion for stimulated emission. Thanks to the well-defined geometries and inherent carrier concentration effect, the microring laser behaved well as an efficient whispering-gallery-mode laser with a very high quality factor (~2600) and low lasing threshold (~13.6 μJ cm^{-2}) simultaneously.

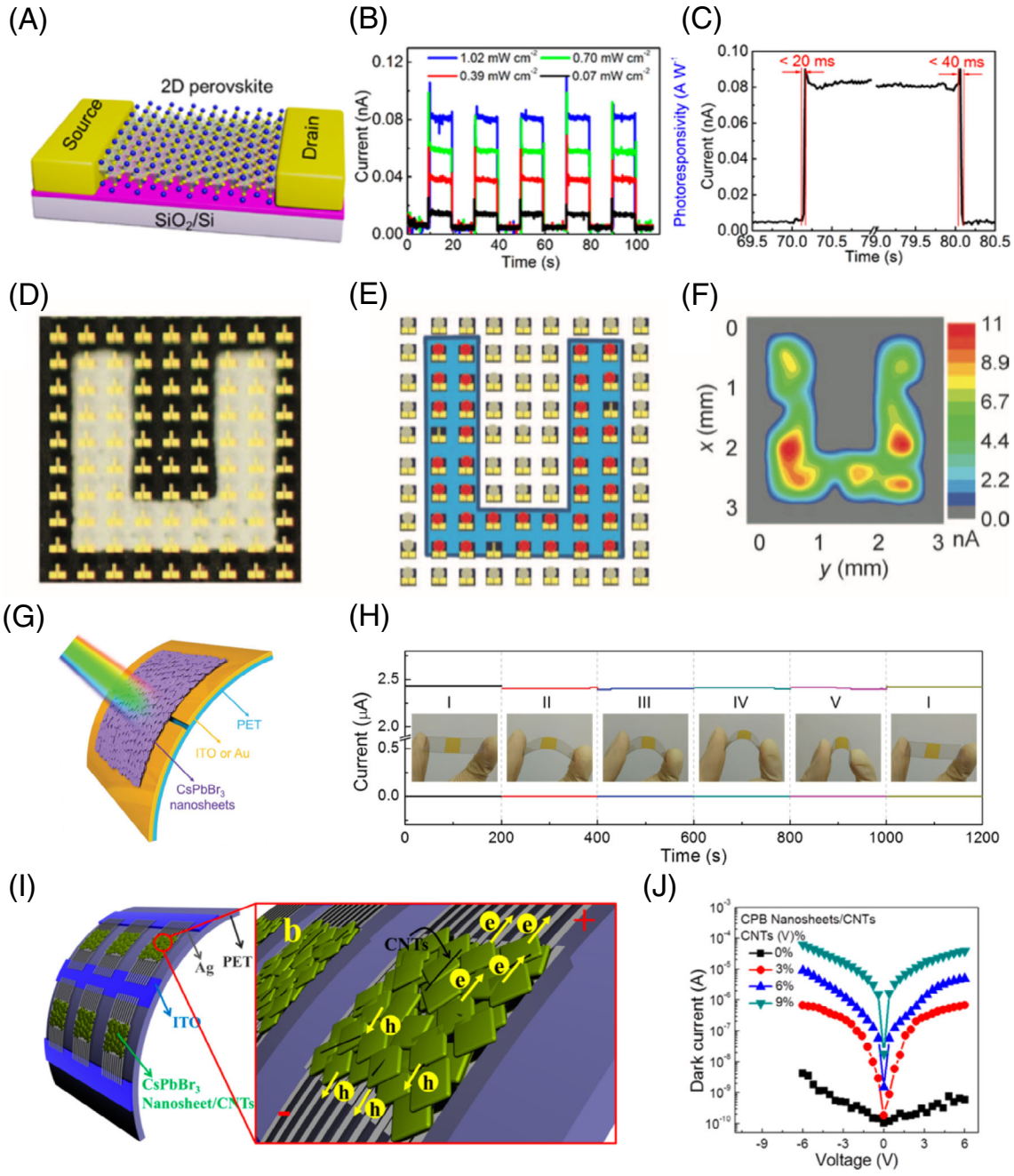

FIGURE 7 A, Schematic of the perovskite nanosheet-based photodetector. B-C, Time-dependent photocurrent and dark current of this perovskite detector. Reproduced with permission.[78] Copyright 2016 American Chemical Society. D, Optical image of photodetector arrays with a U-shaped mask. E, Schematic illustration of the photodetector arrays with a U-shaped mask under blue LED illumination (wavelength, 463 nm; power density, 600 mW cm^{-2}). F, Photocurrent mapping of photodetector arrays with a U-shaped mask under blue LED illumination. Reproduced with permission.[79] Copyright 2015 AAAS. G, Schematic of a flexible photodetector based on $CsPbBr_3$ nanosheets. H, I-t curves of the $CsPbBr_3$ nanosheets-based flexible photodetector bent at different curvatures at a voltage of 5.0 V. The insets are the photographs of the device at different bending states. Reproduced with permission.[161] Copyright 2016 Wiley-VCH. I, The schematic of the photodetector consisted of $CsPbBr_3$ nanosheets and CNTs. J, I-V curves of the photodetector with different amounts of CNTs in dark conditions. Reproduced with permission.[162] Copyright 2017 American Chemical Society

TABLE 3 Summary of key parameters of photodetectors based on low-dimensional perovskites

Materials	Structures	Device configuration	R (A W^{-1}) [bias, light source]	D*(Jones) [bias, light source]	Response time, t_r/t_d	EQE (%)	References
$MAPbI_3$	Nanosheets	Au/Ti/PVSK/Ti/Au	22 [1 V, 405 nm]	N/A	<20 ms/ <40 ms	N/A	78
$MAPbI_3$	Nanosheets	Au/Ti/PVSK/Ti/Au	40 [5 V, 405 nm]	N/A	1.4 s/ 0.09s	N/A	77
BA_2PbBr_4	Nanosheets	Au/Cr/Graphene/ PVSK/Graphene/ Cr/Au	~2100 [0.5 V, 470 nm]	N/A	N/A	N/A	160
$CsPbBr_3$	Nanosheets	ITO/PVSK/ITO	0.64 [10 V, 442 nm]	N/A	19 μs/ 24 μs	54	161
$CsPbBr_3$	Nanosheets	Ag/PVSK/CNTs/Ag	31.1 [10 V, 442 nm]	N/A	16 μs/ 380 μs	7488	162
$CsPbBr_3$	Nanoplatelets	Au/PVSK/Au	34 [1.5 V, 442 nm]	7.5×10^{12} [1.5 V, 442 nm]	0.6 ms/ 0.9 ms	~10^4	163
$BA_2MA_2Pb_3Br_{10}$	Single crystal	Au/PVSK/Au	N/A	3.6×10^{10} [5 V, 420 nm]	150 μs/ 570 μs	~60	164
PEA_2PbBr_4	Single crystal	Au/PVSK/Au	0.03148 [10 V, 365 nm]	1.55×10^{13} [10 V, 365 nm]	0.41 ms/ 0.37 ms	N/A	165
$BA_2MA_3Pb_4I_{13}$	Nanowires	Au/Cr/PVSK/Cr/Au	1.5×10^4 [5 V, 530 nm]	7.5×10^{15} [5 V, 530 nm]	27.6 μs/ 24.5 μs	N/A	54
$MAPbI_3$	Nanowires	Au/PVSK/Au	4.95 [1 V, 530 nm]	2×10^{13} [1 V, 530 nm]	<0.1 ms	N/A	166
$MAPbI_3$	Nanowires	Ag/PVSK/Ag	N/A	N/A	0.12s/ 0.21s	N/A	167
$MAPbI_3$	Nanowires	Pt/PVSK/Pt	0.005 [1 V, 633 nm]	N/A	350 μs/ 250 μs	0.4	168
$MAPbI_3$	Nanowires	Au/PVSK/Au	12 500 [5 V, ~690 nm]	1.73×10^{11} [5 V, 550 nm]	0.34 μs/ 0.42 μs	N/A	169
$MAPbI_3$	Nanowires	Au/PVSK/Au	0.85 [1 V, 650 nm]	2.5×10^{12} [1 V, 650 nm]	~0.3 ms	N/A	170
$MAPbI_3$	Nanowires	ITO/PVSK/Au	~0.035 [0.3 V, 450-780 nm]	~10^{10} [0.3 V, 450-780 nm]	20.47 ms/ 13.81 ms	N/A	171
$CsPbBr_3$	Nanowires	Au/PVSK/Au	4400 [3 V, 405 nm]	N/A	252 μs/ 300 μs	N/A	172
$CsPbBr_3$	Nanowires	Ag/Au/PVSK/Au/Ag	N/A	N/A	~0.1 s	N/A	173

Note: R, responsivity; D*, detectivity; t_r/t_d, rise time/decay time; EQE, external quantum efficiency.

3 | 1D METAL HALIDE PEROVSKITES

As another basic building block, perovskites nanowires or nanorods have been widely investigated for their tunable bandgaps, anisotropic electrical/optical properties, and outstanding photoluminescent efficiency.[168,181-183] In this section, we will go through the progress on the 1D perovskites, including nanowires and nanorods.

3.1 | Synthesis methods

3.1.1 | Solution-phase synthesis method

The first synthesis of metal halide perovskite nanowires ($MAPbI_3$) was demonstrated by the Horváth group in 2014 (Figure 9A-E).[168] Two sets of $MAPbI_3$ nanowires with mean diameters of 50 and 400 nm and lengths up to 10 μm were fabricated by a solution-mediated crystallization process (Figure 9F-I). A thin saturated solution film

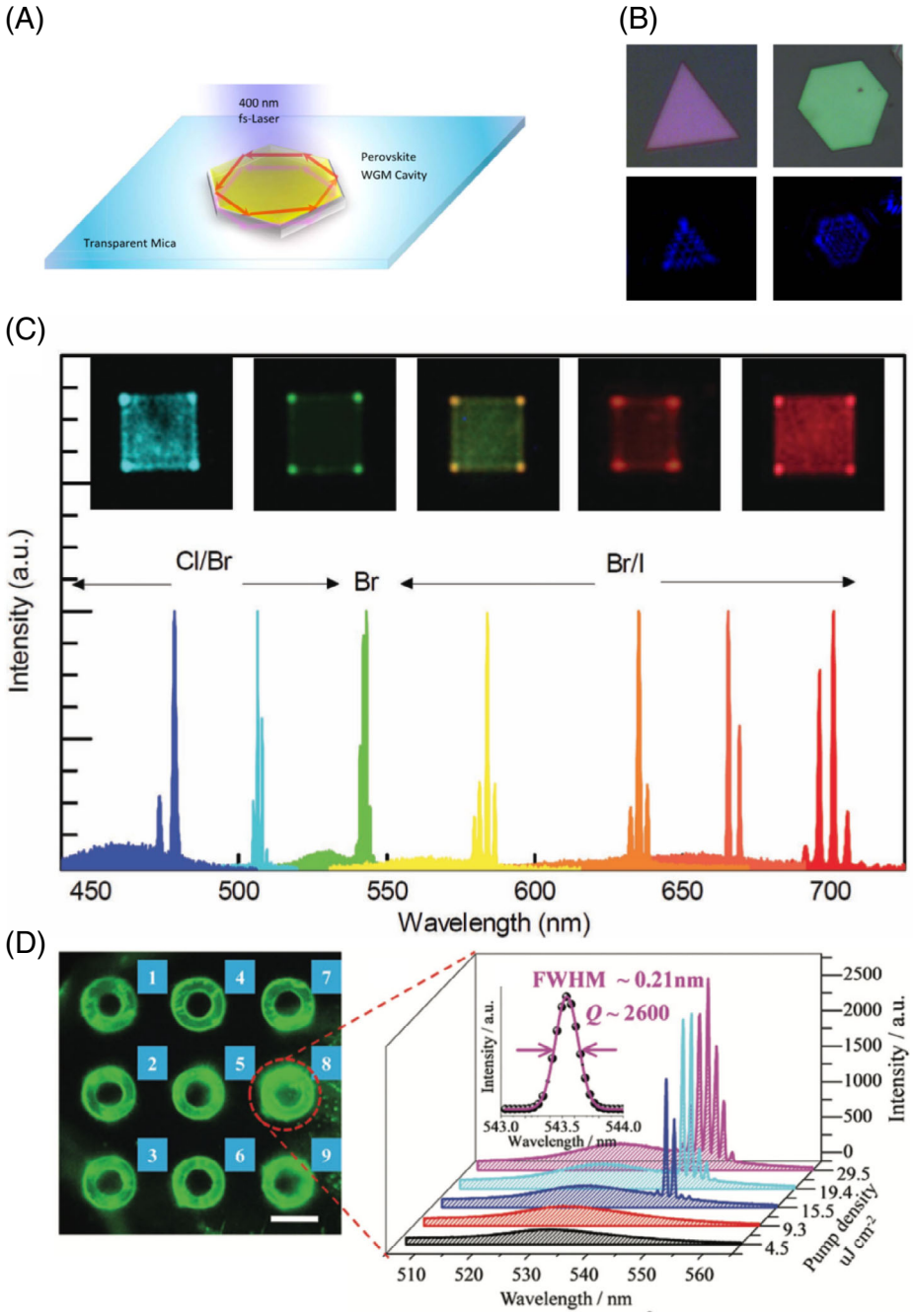

FIGURE 8 A, Schematic of the $MAPbX_3$ perovskite nanoplatelet-based laser. The whispering-gallery-mode is illustrated in these nanoplatelets. B, Optical images of two $CH_3NH_3PbI_3$ nanoplatelets under the illumination of white light (upper) and incidence laser (bottom). Clear diffraction patterns can be seen inside the whispering-gallery-mode cavity. Reproduced with permission.[176] Copyright 2014 American Chemical Society. C, Lasing spectra from $CsPbX_3$ nanoplatelets with different compositions. The insets are photographs of the corresponding lasers. Reproduced with permission.[179] Copyright 2016 Wiley-VCH. D, Photoluminescence (PL) images of 3 × 3 microring laser arrays. Spatial interference patterns from all the microrings indicate the coherent outputs. The right figure shows the PL spectra of the ring labeled as 8 vs pump intensity. Reproduced with permission.[180] Copyright 2018 Wiley-VCH

of $MAPbI_3$ in DMF was confined by two glass slides, and the nanowires came into crystallization while gradually sliding the upper glass to expose the liquid to air. It was assumed that the nanowire growth was due to the directional effect of DMF that an internal complex with the methylamine group was formed during the crystallization process.[116,167,188,189] A great breakthrough in halide perovskite nanowire synthesis was put forward by

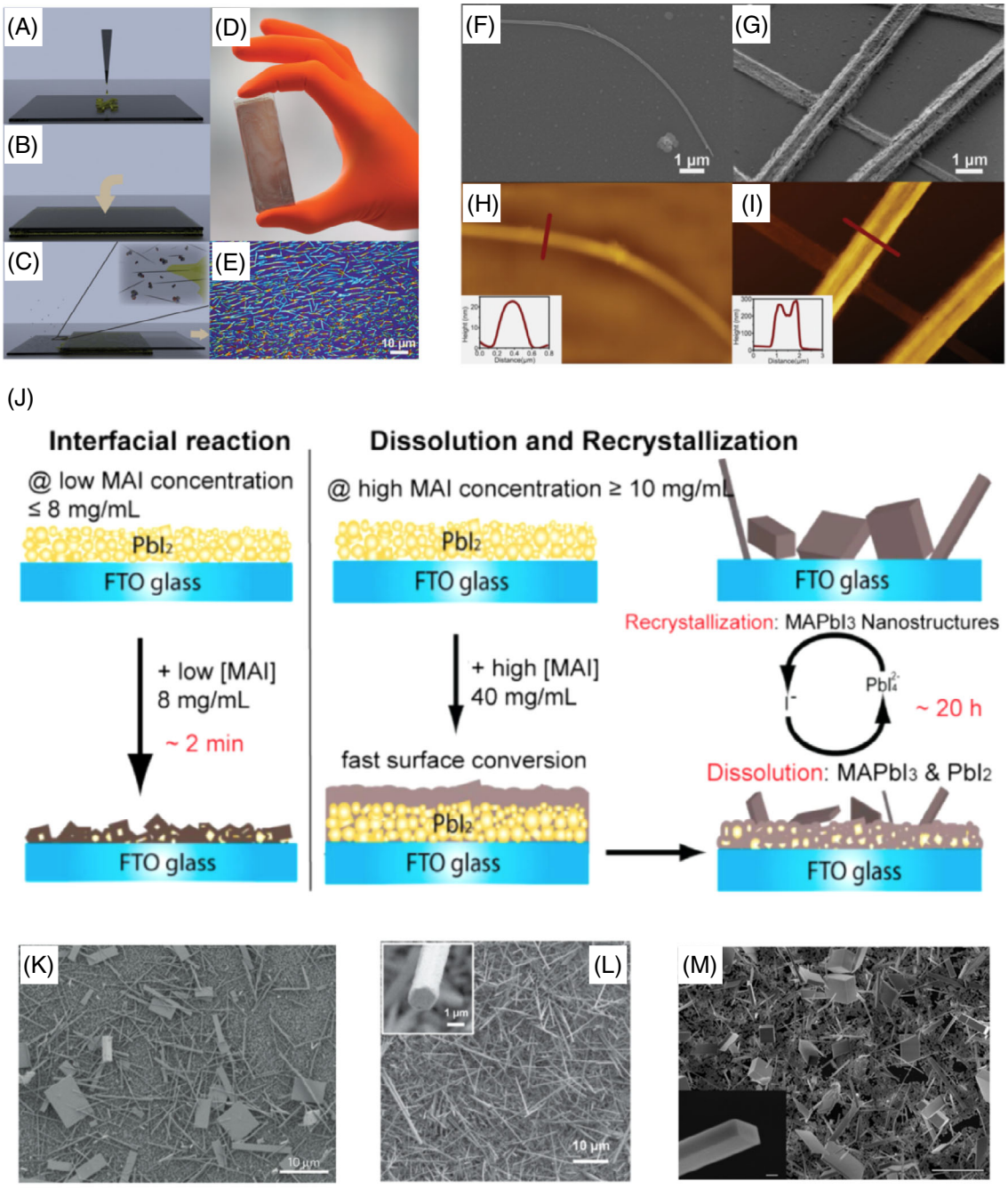

FIGURE 9 A-E, Schematic illustration of the solution synthesis of $MAPbI_3$ nanowires by glass slides. F-I, Scanning electron microscope (SEM) (F-G) and AFM (H-I) images of $MAPbI_3$ nanowires with different diameters. Reproduced with permission.[168] Copyright 2014 American Chemical Society. J, Schematic illustration of two growth modes of perovskite nanostructures. Left: interfacial reaction mechanism at lower MAI concentration, right: dissolution-recrystallization growth mechanism at higher MAI concentration. Reproduced with permission.[184] Copyright 2015 American Chemical Society. K, SEM image of $MAPbI_3$ perovskite nanowires and nanoplatelets through the dissolution-recrystallization growth method. Reproduced with permission.[185] Copyright 2015 Nature Publishing Group. L, SEM image of $FAPbI_3$ nanowires and nanoplatelets synthesized from the dissolution-recrystallization growth method. The inset is the top-view SEM image of the $FAPbI_3$ nanowire. Reproduced with permission.[186] Copyright 2016 American Chemical Society. M, SEM image of $CsPbBr_3$ nanowires and nanoplatelets grown from PbI_2 in a CsBr/methanolic solution (Scale bar, 10 μm). The inset is a cross-sectional SEM image of the corresponding nanowire (Scale bar, 500 nm). Reproduced with permission.[187] Copyright 2016 National Academy of Sciences

Fu et al. (Figure 9J)[184] They proposed a dissolution-recrystallization model to grow single-crystalline $MAPbI_3$ nanowires. The pre-deposited poly-crystalline lead iodide (PbI_2) film was immersed into MAI/isopropanol solution with different concentrations, where high concentration will lead to the formation of thermodynamically

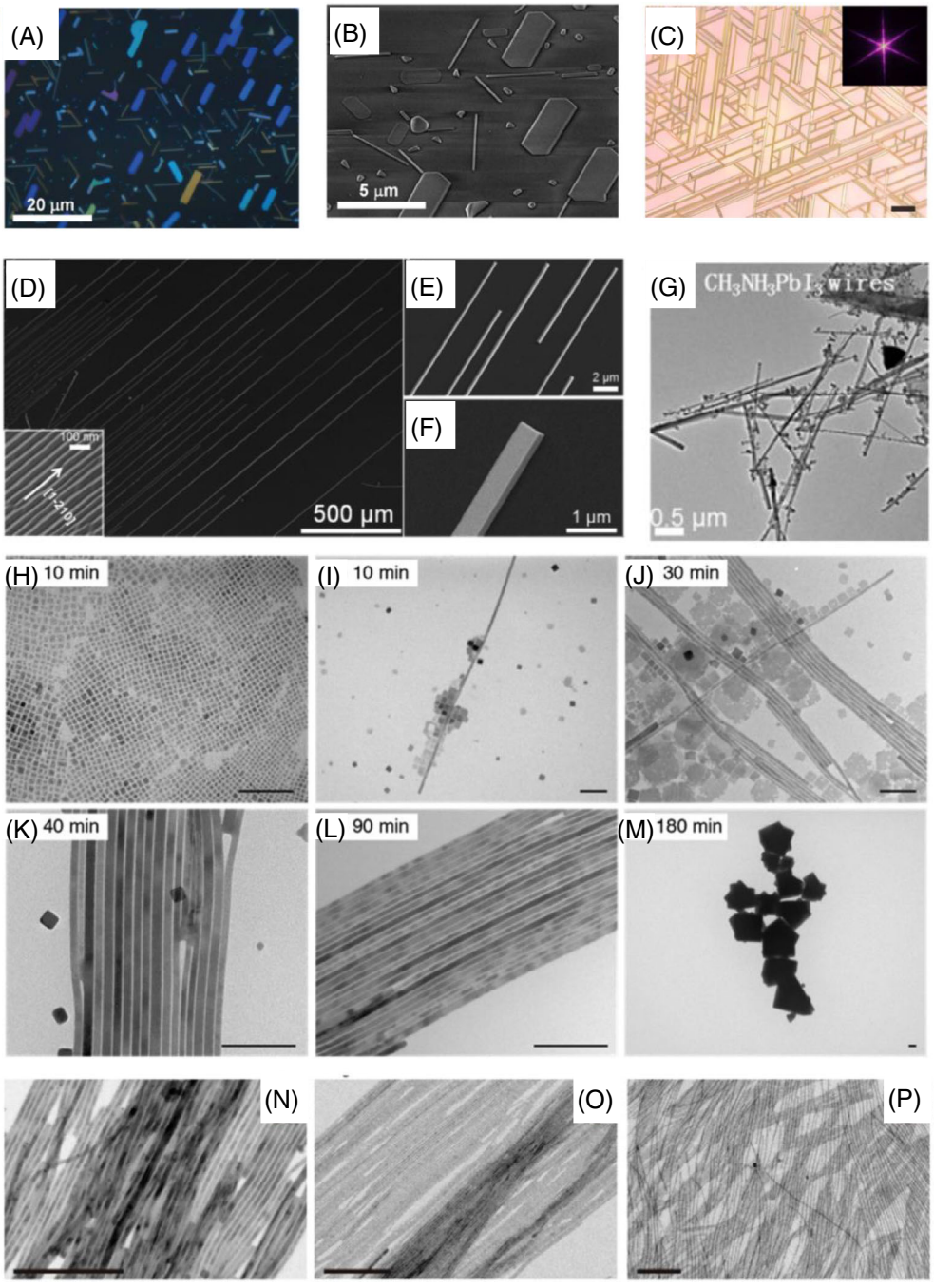

FIGURE 10 A-B, Optical images and scanning electron microscope (SEM) images of lead halide nanostructures from the vapor-phase synthesis method. Reproduced with permission. [75] Copyright 2014 Wiley-VCH. C, Optical images of $CsPbBr_3$ wire networks grown on phlogopite mica from the vapor-phase synthesis method (Scale, 10 μm). The inset is the corresponding 2D Fast Fourier Transform image. Reproduced with permission.[173] Copyright 2016 American Chemical Society. D-F, SEM images of the vapor-synthesized ultralong $CsPbBr_3$ nanowires grown along M-plane sapphire at different magnifications. Reproduced with permission.[172] Copyright 2017 American Chemical Society. G, Transmission electron microscope (TEM) images of $MAPbI_3$ nanowires obtained through a colloidal synthesis method. Reproduced with permission.[199] Copyright 2015 American Chemical Society. H-M, TEM images of the shape evolution of $CsPbBr_3$ nanostructures at different reaction stages (Scale bar, 100 nm). Reproduced with permission.[190] Copyright 2015 American Chemical Society. N-P, $CsPbBr_3$ nanowires with different diameters synthesized by controlling the precursor ratio in a colloidal synthesis method. Reproduced with permission.[200] Copyright 2016 American Chemical Society

favorable PbI_4^{2-} complex ions after reacting with superficial $MAPbI_3$ and PbI_2. As PbI_4^{2-} ions became oversaturated, they would react with MA^+ and facilitate the anisotropic growth of nanostructures (Figure 9K).[185] Starting from this method, different kinds of perovskite nanowires were successfully synthesized. For example, stabilized $FAPbI_3$ nanowires (Figure 9L) and robust inorganic $CsPbX_3$ nanowires (Figure 9M) were both successfully demonstrated by modifying the precursor compositions and concentrations feasibly.[186,187,190-194]

3.1.2 | Vapor-phase synthesis method

In the past years, the vapor-phase synthesis method was widely used to fabricate high-quality all inorganic nanowires like silicon, tin oxide, and zinc oxide and was then modified for the perovskite nanowire synthesis.[195-198] In 2014, Ha et al. successfully demonstrated $MAPbX_3$ perovskite nanowires through a two-step vapor phase method, where lead halide (PbX_2) nanowires were first deposited by CVD (Figure 10A-B) and then converted into perovskite through the gas-solid reaction with amine halide molecules.[75] Compared to this with two processes, direct vapor-phase growth is also effective for nanowire fabrication. It is commonly used for traditional inorganic nanowire synthesis and unsuitable for organic halide perovskite with low decomposition temperature. However, when applied to all inorganic thermal-stable halide perovskite, this approach will become more feasible.[172,173,201] Chen et al. reported a vapor-phase epitaxial growth of horizontal single-crystalline $CsPbX_3$ nanowires and microwires with controlled crystallographic orientations.[173] The asymmetric lattice mismatch between $CsPbX_3$ and mica substrates leads to strict growth along the [110] direction and unlimited growth along the [001] direction, forming different morphologies such as single nanowires, Y-shaped branches, interconnected nanowire, or microwire networks (Figure 10C). Later, based on a similar direct vapor-phase synthesis, Shoaib et al. fabricated ultralong $CsPbBr_3$ nanowires (Figure 10D-F), induced by graphoepitaxial effect on M-plane sapphire substrates, with diameters of several hundred nanometers and lengths up to several millimeters.[172]

3.1.3 | Colloidal synthesis method

The successful appliance of the colloidal method on the synthesis of perovskite quantum dots promotes it to the fabrication of perovskite nanowires. The first colloidal synthesis was based on an antisolvent precipitation method. Zhu et al. dissolved PbX_2, MAX, and long-chain $CH_3(CH_2)_7NH_3X$ (X = Cl/Br/I) in a polar solvent (such as ACN) and added the mixture into a solvent with lower polarity (such as toluene), obtaining perovskite nanowires with precise control (Figure 10G).[199] When switching to inorganic nanowires, representative works employing the hot-injection method were performed by Zhang et al.[190-192] Through injecting the cesium precursor into the PbX_2 solution in the presence of oleylamine and oleic acid at 150°C-250°C, they demonstrated the fabrication of inorganic $CsPbX_3$ nanowires for the first time (Figure 10H-M)[190] and controlled the compositions and diameters in their subsequent work, enabling these nanowires potential candidates for optoelectrical applications.[191,192] Afterward, colloid synthesis methods were further investigated with more precise control. For instance, Imran et al. prepared size-tunable $CsPbBr_3$ nanowires by introducing carboxylic acids with short aliphatic chains (Figure 10N-P).[200] High PL quantum yield up to 77% and color tunability from blue to green were both obtained in these colloidally synthesized nanowires.

3.1.4 | Templated synthesis method

Using a template that confines the precursor to form the desired structures seems to be straightforward. Ashley et al. fabricated $MAPbI_3$ nanowires by selecting an AAO membrane as the template (Figure 11A).[202] They drop-cast perovskite precursor into the AAO pores and followed with an annealing process to enable the formation. One obvious advantage here is the amenable diameter control by selecting varisized AAO templates. In their demonstration, $MAPbI_3$ nanowires with diameters ranging from 50 to 200 nm, with a dispersity less than 10%, were synthesized readily. Later, Waleed et al. combined the vapor-phase process with this template confinement method, fabricating lead-free and inorganic perovskite nanowires with a start from pure metals (Figure 11B).[203,205] To be specific, AAO membranes were still chosen as the template, and metal tin or lead was electrochemically deposited in the bottom of the nanopores. MAI or CsI gas, produced by heating the corresponding powders, were transported by the carrier gas and reacted with the as-deposited metal, facilitating the forming of final $MASnI_3$ or $CsPbI_3$ nanowires (Figure 11B,C).[203] Oener et al. devised a nanowire extrusion method where precursor was first dropped on the AAO templates with double-sided pores. Then a reduced pressure by a syringe was applied to enable the precursor to fill in the pores of the template and extrude out on the

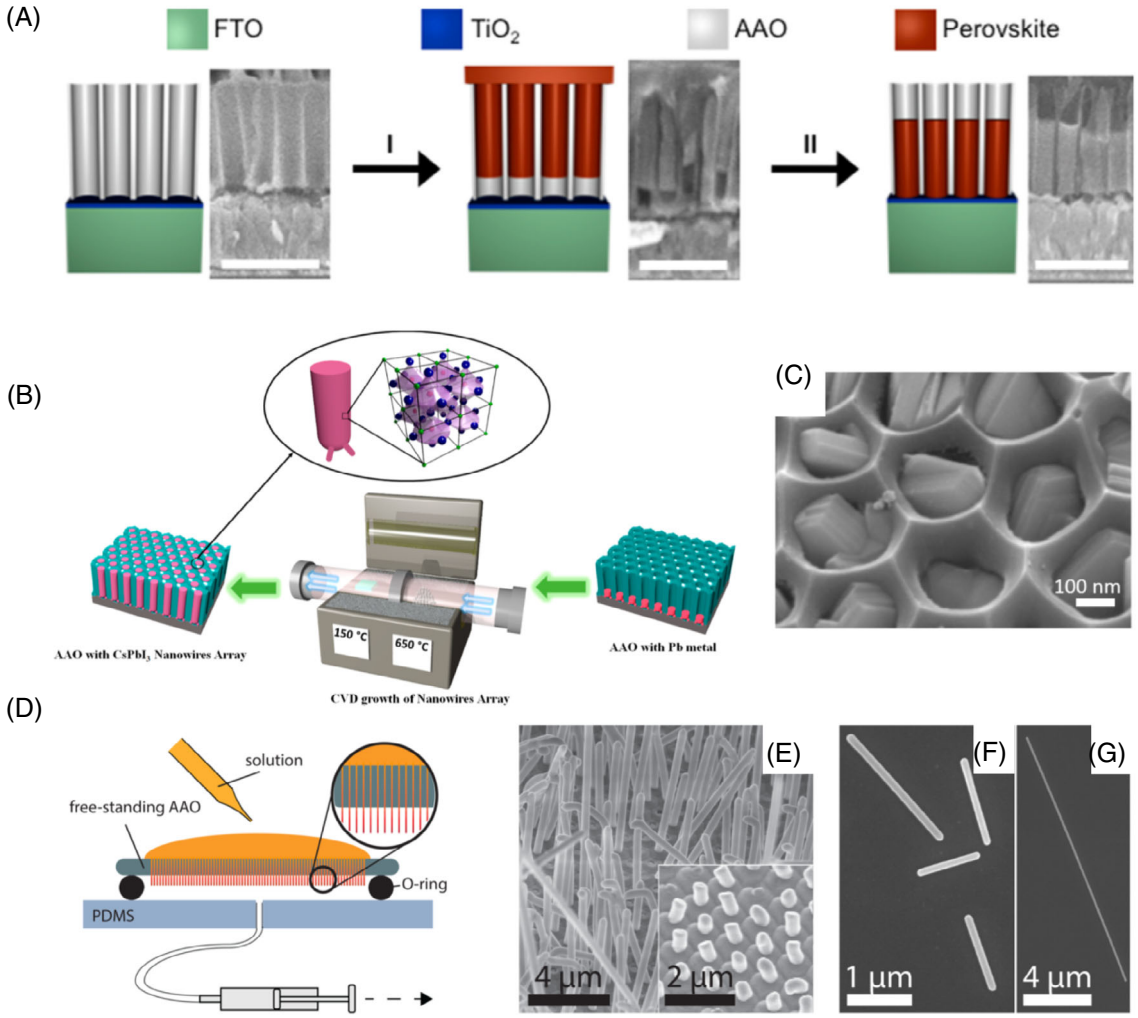

FIGURE 11 A, Schematic of AAO template-assisted synthesis of perovskite nanowires. Reproduced with permission.[202] Copyright 2016 American Chemical Society. B, Schematic of the templated synthesis of $CsPbI_3$ nanowires starting from pure metal lead. C, Top-view scanning electron microscope (SEM) image of $CsPbI_3$ nanowires inside the AAO templates. Reproduced with permission.[203] Copyright 2017 American Chemical Society. D, Schematic illustration of the extrusion process of $MAPbBr_3$ nanowires with the assistance of the AAO template. E, SEM image of vertical aligned $MAPbBr_3$ nanowires. The inset shows short nanowires by controlling of the fabrication time. F-G, SEM images of nanowires with different lengths at high magnifications. Reproduced with permission.[204] Copyright 2017 American Chemical Society

bottom (Figure 11D).[204] Transfer of the template onto glass spacers positioned on a hot plate would remove the solvent residue and promote the final formation of $MAPbBr_3$ nanowires (Figure 11E-G).

3.2 | Applications of 1D metal halide perovskites

3.2.1 | Lasers

Anisotropic nanowires can serve as a waveguide along the axial direction, and the two end facets can form a Fabry-Perot cavity for optical amplification.[187,206] Therefore, the single-crystalline perovskite nanowires with ideal facets are good candidates for the optically pumped lasers. The first lead halide perovskite nanowire-based laser was demonstrated by Zhu et al. (Figure 12A) from a room-temperature solution method, showing wavelength-tunable lasing with very low thresholds (220 nJ cm^{-2}) and a high-quality factor (Q ~ 3600) (Figure 12B).[185] The further analysis estimated that the lasing quantum yield approaches 100% due to little charge carrier trapping in these nanowires. Using a similar solution method, nanowire lasers based on $FAPbI_3$ and their stabilized alloys were proposed by the same group (Figure 12C).[186] The lasers exhibited durable lasing under

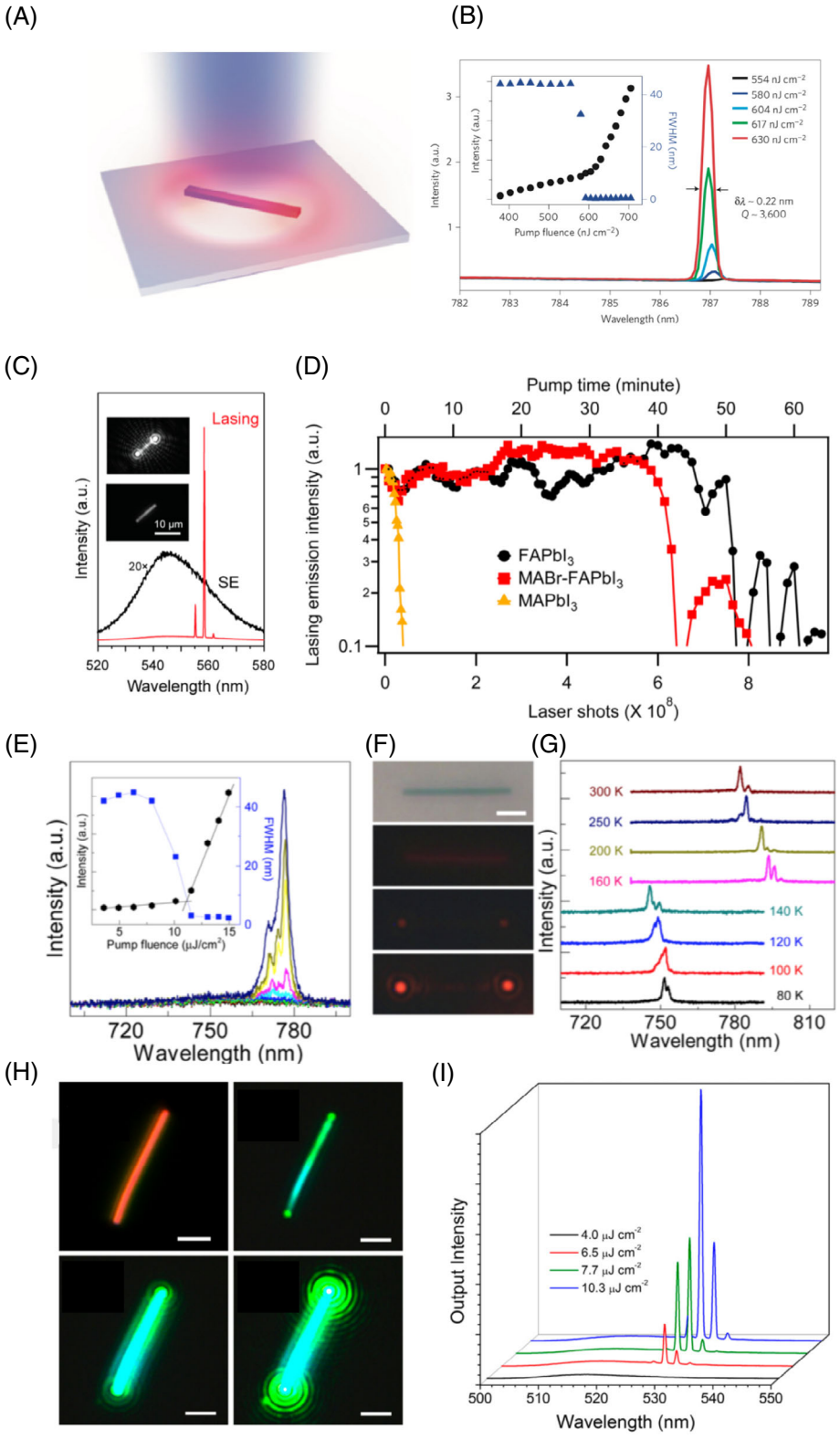

FIGURE 12 Legend on next page.

~10^8 shots of sustained illumination of pulsed laser excitation, substantially exceeding the stability of $MAPbI_3$ (~10^7 shots) (Figure 12D). In addition to the solution process, vapor-phase synthesized nanowires were also suitable for nanolasers.[174] The optically pumped $MAPbI_3$ nanowire lasers exhibited a wavelength of 777 nm, a threshold of 11 μJ cm^{-2}, and a quality factor of 405 (Figure 12E-G). In consideration of the stability issue, Eaton et al. first moved their eyesight onto inorganic $CsPbX_3$ nanowire-based nanolasers (Figure 12H).[187] Compared to the organic counterparts, the inorganic metal halide nanowires showed robust property without sacrificing high emitting performance (Figure 12I). Low lasing threshold, high-quality factors, and robust stability under ambient conditions render the inorganic nanowires a promising platform for nanophotonic integrity.

3.2.2 | Solar cells

Due to the enhanced mechanical property and better conduction in specific directions, perovskite nanowires are also explored as absorber in solar cells.[116-121] Park et al. first incorporated $MAPbI_3$ nanowires into the solar cell (Figure 13A) and investigated its optical and electrical properties.[116] Compared to the nano-cubic counterparts, higher lateral conductivity was observed in nanowires, revealing a better connecting pathway. Time-resolved fluorescence spectroscopy confirmed that hole extraction from the nanowires was more efficient than that in the bulk case, mainly due to the better contact with hole transport materials from increased surface area. As a result, an improved PV performance with the best PCE of 14.71% was proved in nanowire-based solar cells (Figure 13B). Since then, a series of solar cells based on $MAPbI_3$ perovskite nanowires have emerged with modified fabrication processes (Figure 13C). A PCE of 18.83% with long-term stability was achieved through an integrated approach by Chang et al. (Figure 13D).[117] In 2017, Kuang et al. fabricated solar cells based on $CsPbX_3$ nanowires with enhanced thermal and humidity stability compared to organic counterparts.[120] The $CsPbI_3$ and $CsPbBr_3$ nanowire-based solar cells yielded the PCEs of 0.11% and 1.21%, respectively (Figure 13E). An impressive work was done in lead-free perovskites where Chen et al. synthesized high-quality $CsSnX_3$ (X = Cl/Br/I) nanorods for solar cell absorbers (Figure 13F). A PCE up to 12.96% under AM 1.5G has been achieved, revealing the potential of Sn-based perovskite nanorods in solar cell applications (Figure 13G).[121] A summary of the key parameters of solar cells based on 1D perovskites is exhibited in Table 1.

3.2.3 | Light-emitting diodes

In 2015, through a solution method, Wong et al. successfully synthesized $MAPbBr_3$ perovskite nanorod arrays (Figure 14A),[149] which were further converted into $MAPbI_3$ nanorods by an anion exchange reaction. Both types of nanorod arrays were applied as the active layer in LED devices (Figure 14B) and exhibited electroluminescent at room temperature (Figure 14C). Compared to thin films, the vertically oriented nanorod arrays offers several advantages, such as large active surface area, high carrier injection efficiency, and improved strain relaxation from thermal expansion. In their work, the $MAPbBr_3$ nanorod-based LED showed green EL at 532 nm with a full width at half maximum (FWHM) of 26 nm (Figure 14D) and the converted $MAPbI_3$ arrays showed infrared EL at 782 with an FWHM of 41 nm. This work demonstrates the potential of large-scale nanorod fabrication in LED applications.

3.2.4 | Photodetectors

In 2014, Horvath did the pioneering work of perovskite nanowire-based detectors (Figure 15A).[168-170,208-212] Although the responsibility of this detector is 5 mA W^{-1}, 4 orders of magnitude smaller than that of state-of-art

FIGURE 12 A, Schematic of a perovskite nanowire on SiO_2 substrate pumped by the laser excitation. B, Emission spectra of $MAPbI_3$ nanowires at the intensities around the lasing threshold. Inset: integrated emission intensity and full width at half maximum (FWHM) as functions of excitation intensity. Reproduced with permission.[185] Copyright 2015 Nature Publishing Group. C, Emission spectra of a $FAPbI_3$ nanowire with the excitations below and above the lasing threshold. Inset: optical images the nanowire below and above the lasing threshold. D, Lasing intensity of $FAPbI_3$, MABr-stabilized $FAPbI_3$, and $MAPbI_3$ nanowires as a function of pump time under continuous illumination of 402 nm pulsed laser. Reproduced with permission.[186] Copyright 2016 American Chemical Society. E, Emission spectra of vapor-phase synthesized $MAPbI_3$ nanowire at the pump densities around the lasing threshold. Inset is the emission intensity as a function of pump intensity. F, Optical images of the $MAPbI_3$ nanowire under different pump densities. G, Lasing spectra of a single $MAPbI_3$ nanowire at different temperatures. Reproduced with permission.[174] Copyright 2015 American Chemical Society. H, Optical images of $CsPbBr_3$ nanowires under different excitation densities (Scale bars, 2 μm). I, Power-dependent emission spectra of $CsPbBr_3$ nanowires. Reproduced with permission.[187] Copyright 2016 National Academy of Sciences

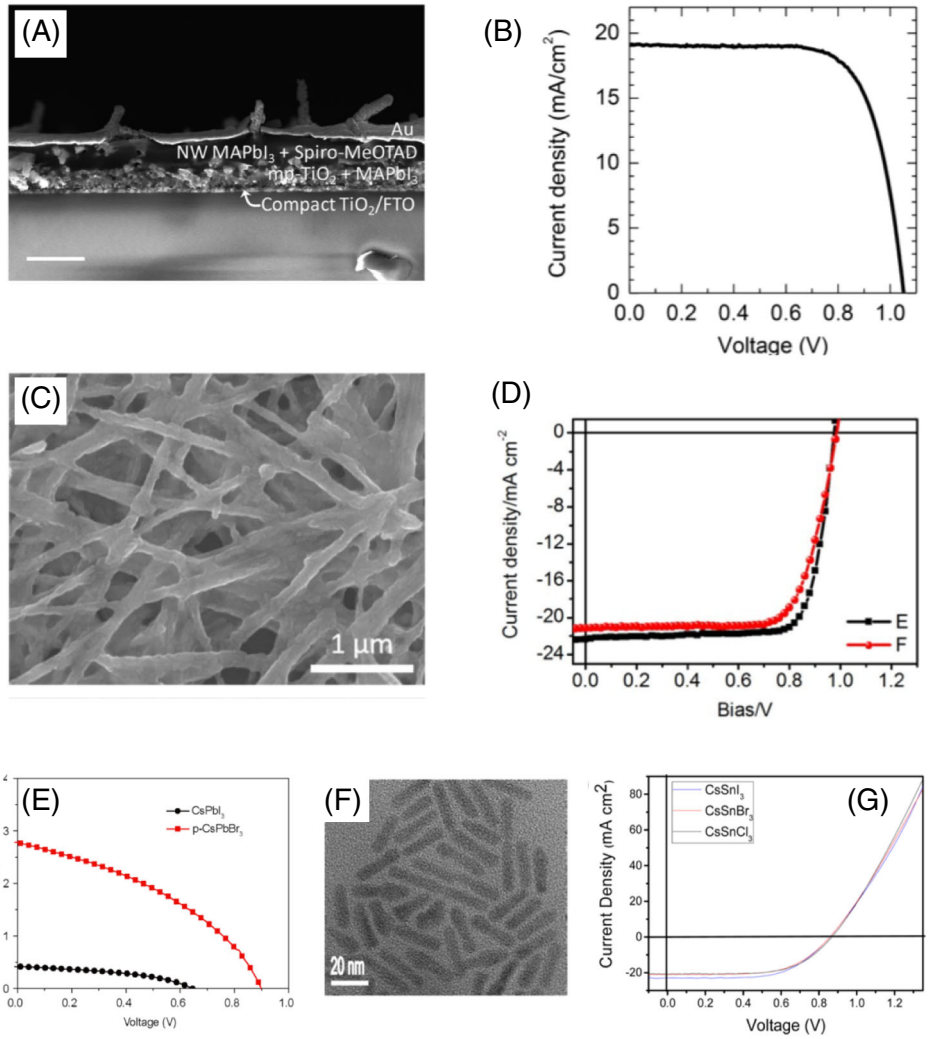

FIGURE 13 A, Cross-sectional scanning electron microscope (SEM) image of a solar cell based on $MAPbI_3$ nanowires. B, J-V curves of the corresponding perovskite nanowire-based solar cell, showing a power conversion efficiency (PCE) of 14.71%. Reproduced with permission.[116] Copyright 2015 American Chemical Society. C, SEM image of $MAPbI_3$ perovskite nanowires. D, J-V curves of $MAPbI_3$ nanowire-based large-area solar cells under simulated AM 1.5G solar illumination (100 mW/cm^2). The black curve refers to the device with an active area of 1.2 cm^2, and the red curve refers to the device with an active area of 5.04 cm^2. Reproduced with permission.[117] Copyright 2017 The Royal Society of Chemistry. E, J-V curves solar cells based on $CsPbI_3$ nanowires and $CsPbBr_3$ nanowires under one-sun illumination. Reproduced with permission.[120] Copyright 2017 Science China Press and Springer-Verlag Berlin Heidelberg. F, High-resolution transmission electron microscope (TEM) image of lead-free perovskite $CsSnI_3$ quantum rods. G, J-V curves of perovskite solar cells based on $CsSnI_3$, $CsSnBr_3$, and $CsSnCl_3$ quantum rods. Reproduced with permission.[121] Copyright 2016 American Chemical Society

detectors made from monolayer graphene, the response times (rise and decay times) were within 500 μs, ~10^4 faster than that of graphene-based detectors (Figure 15B).[213-216] The photocurrent-dark current ratio and EQE at low voltages (<0.5 V) both showed superior performance than that based on their nanoparticle form, mainly arising from the reduced grain boundaries, which permit smooth carrier flowing channels in transport. In addition to these merits, enhanced absorption and mechanical integrity are other outstanding advantages. Zhu et al. demonstrated a $MAPbI_3$ nanowire-based photodetector on a flexible substrate from a post-solution treatment, revealing a 10% increase in absorption and enhanced mechanical property compared to thin-film based one (Figure 15C).[167] Utilizing the morphological anisotropy of nanowires, Gao et al. demonstrated a photodetector with high polarization sensitivity and detectivity (2×10^{13} Jones) for the first time.[166] Considering the instability issues, several groups moved interests onto the inorganic counterparts.[192,203] Waleed et al. used the AAO templates to fabricate $CsPbI_3$ nanowire-based photodetector, showing high stability when stored in organic polar solvents for 30 days.[203] Zhang et al. formed a

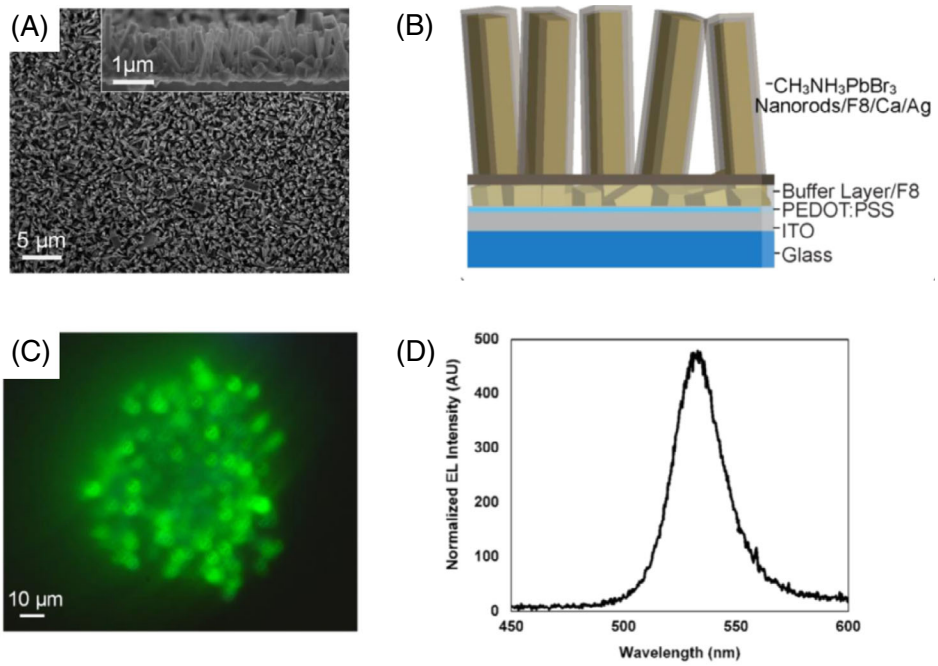

FIGURE 14 A, Top-view scanning electron microscope (SEM) of as-synthesized $MAPbBr_3$ nanorods. Inset is the cross-sectional SEM image of the $MAPbBr_3$ nanorods. B, Device structure of an light-emitting diode (LED)-based on $MAPbBr_3$ nanorod arrays. C, Photograph of electroluminescence (EL) from the $MAPbBr_3$ nanorod array LED. D, EL spectrum of the $MAPbBr_3$ nanorod array LED. Reproduced with permission.[149] Copyright 2015 American Chemical Society

thin $CsPbBr_3$-nanowires based photodetector, showing a sensitive photoresponse (Figure 15D).[192] For practical spatial image applications, individual photodetectors should be integrated into arrays for graphic detection. Deng et al. demonstrated photodetector arrays for image mapping by synthesizing perovskite networks on poly(ethylene terephthalate) substrates.[207] These arrays consisted of 49 individual detectors and could obtain a clear mapping of light source (Figure 15E). In the later work, Gu et al. increased the number of pixels to 1024 in each image sensor using well-aligned nanowires by a templated method discussed above (Figure 15F). The still images and videos could be well captured by these high-resolution nanowire arrays (Figure 15G).[171] For further comparison, we summarize the key parameters of photodetectors based on 1D perovskites in Table 3.

4 | 0D METAL HALIDE PEROVSKITES

4.1 | Synthesis methods

4.1.1 | Ligand-assisted precipitation method

In 2014, for the first time, Schmidt et al. synthesized $MAPbBr_3$ nanocrystals (Figure 16A) by reacting the mixture of MABr and a long-chain alkyl ammonium bromide with $PbBr_2$ in the presence of oleic acid and octadecene.[217] The nanoparticles were then precipitated by the addition of acetone and centrifugation. The as-synthesized nanoparticles exhibited diameters of ~6 nm and a strong PL intensity around 525 nm. Later, this method was adopted by several groups with further modification.[218,219] For example, Zhang et al. produced brightly luminescent $MAPbBr_3$ nanocrystals with absolute PLQY up to 70% by the incorporation of n-octylamine and oleic acid as ligands (Figure 16B-D).[218] The nanocrystals show an average size of 3.3 nm and binding energy to ~350 meV. Wei et al. synthesized perovskite nanocrystals by a homogeneous reaction in various nonpolar organic solvents (Figure 16E-G).[219] Notably, this approach could be conducted in the open air and further extended to a gram level.

4.1.2 | Hot-injection method

In addition to ligand-assisted precipitation, hot-injection is another efficient method to synthesize monodisperse perovskite nanocrystals.[220-223] Inorganic $CsPbX_3$ nanocrystals were achieved (Figure 17A-C) by the injection of cesium oleate into a mixed solution of PbX_2, oleic acid, and oleylamine in a high boiling solvent (octadecene) at

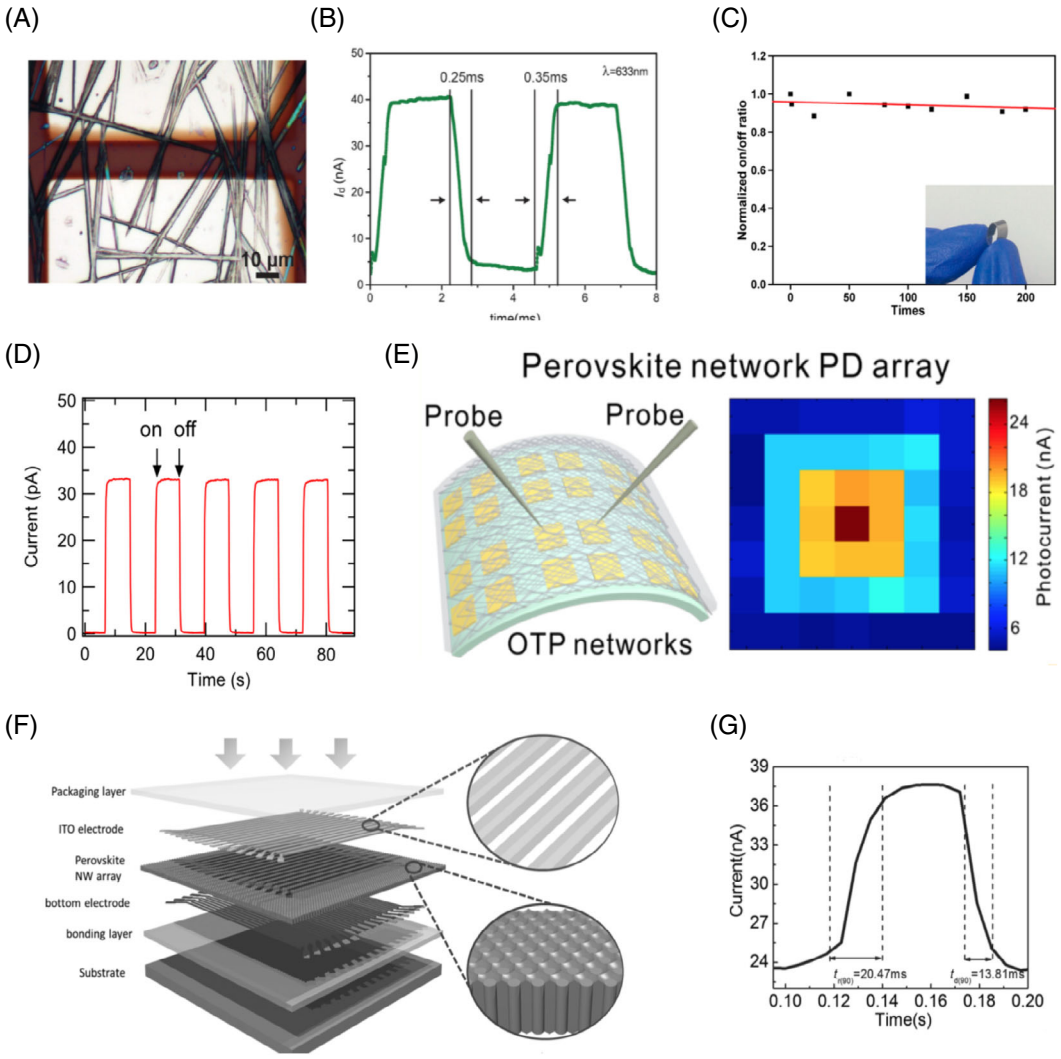

FIGURE 15 A, Optical image of the $MAPbI_3$ nanowire-based photodetector where the perovskite nanowires cross the Pt electrodes. B, Time-resolved photocurrent and dark current of the $MAPbI_3$ nanowire-based photodetector (illumination wavelength: 633 nm). Reproduced with permission.[168] Copyright 2014 American Chemical Society. C, On/off ratio vs bending times of the $MAPbI_3$ nanowire-based flexible photodetector. The inset is the photograph of the flexible detector. Reproduced with permission.[167] Copyright 2016 American Chemical Society. D, Photoresponse of a $CsPbBr_3$ nanowire-based device under a voltage bias of 2 V. Reproduced with permission.[192] Copyright 2014 American Chemical Society. E, Left is the schematic of a flexible $MAPbI_3$ network-based photodetector array. Right is the spatial distribution mapping of light source intensity of the array with 49 photodetectors. The four colors denote the four light power densities of 10, 40, 80, and 100 μW cm^{-2}, respectively. Reproduced with permission.[207] Copyright 2015 American Chemical Society. F, Layer-by-layer structure of 32 × 32 $MAPbI_3$ nanowire-based image sensor. G, Photoresponse of the single pixel under the light of 6 mW cm^{-2} and a voltage of 3 V. Reproduced with permission.[171] Copyright 2016 Wiley-VCH

140°C-200°C.[220] The synthesized nanocrystals showed stable, narrow, and broadly tunable photoluminescence with a quantum yield of 50%-90%. Subsequently, a low-temperature, partial/complete anion-exchange in $CsPbX_3$ nanocrystals was demonstrated by the same group (Figure 17D).[221] The emission could cover the visible spectral region (410-700 nm) by reacting with suitable reagents in the precursors (Figure 17E). An inter-nanocrystal anion-exchange was further proposed, which could achieve $CsPbCl_xBr_{3-x}$ or $CsPbBr_xI_{3-x}$ compositions by readily mixing $CsPbCl_3$, $CsPbBr_3$, and $CsPbI_3$ nanocrystals in proper ratios (Figure 17F).

4.1.3 | Template-assisted method

Similar to 2D or 1D nanostructure fabrication, the template-assisted method is also suitable for perovskite nanocrystal synthesis. Kojima et al. demonstrated the $MAPbBr_3$ nanocrystal synthesis using a mesoporous alumina oxide in 2012

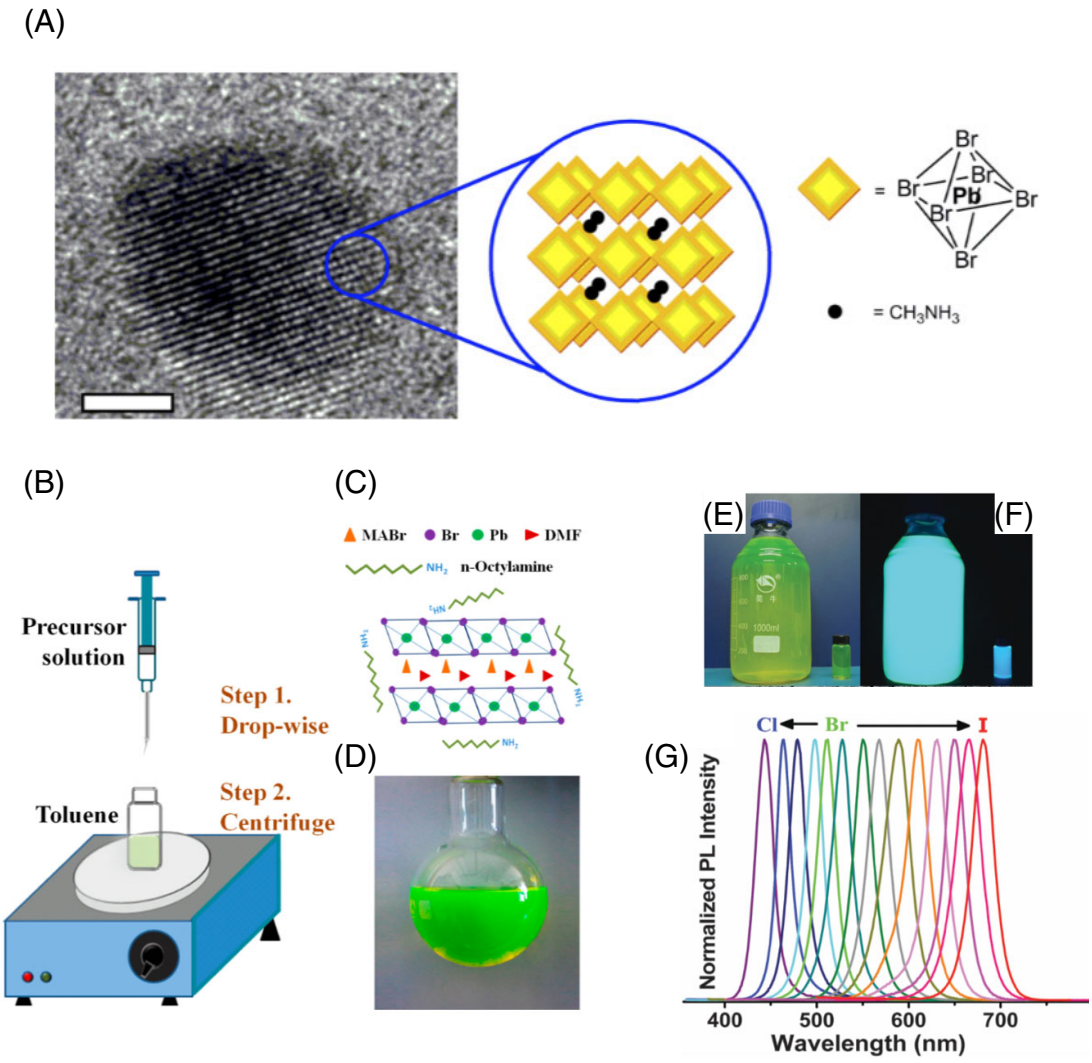

FIGURE 16 A, High-resolution transmission electron microscope (TEM) image of an isolated $MAPbBr_3$ quantum dot synthesized from precipitation method. The inset is the structure of the $MAPbBr_3$ perovskite. Reproduced with permission.[217] Copyright 2014 American Chemical Society. B, Schematic of the synthesis process of ligand-assisted reprecipitation method. C, Schematic illustration of starting materials in the precursor. D, Photograph of colloidal $MAPbBr_3$ quantum dot solution. Reproduced with permission.[218] Copyright 2015 American Chemical Society. E-F, Photograph of $CsPbBr_3$ nanocrystal solution under indoor light and UV light illumination. G, Photoluminescence (PL) spectra of $CsPbX_3$ (X = Cl, Br, I) nanocrystals covering a wide color range. Reproduced with permission.[219] Copyright 2016 The Royal Society of Chemistry

(Figure 18A).[224] The $MAPbBr_3$ nanocrystals were formed on porous Al_2O_3 film due to a rapid self-organized process after the dry of solvents. In 2015, Longo et al. utilized Al_2O_3 nanocrystals, with which MABr and $PbBr_2$ were mixed, to prepare perovskite nanocrystals with high PLQY.[227] Spin-coating the mixture on a glass/quartz substrate and annealing the sample, the perovskite nanocrystals were formed with Al_2O_3 particles surrounding. The dimensions of perovskite nanocrystals were precisely governed by the sizes and concentrations of alumina nanoparticles. In addition, porous silica could also be used as templates. Malgras (Figure 18B-D) and Dirin et al. (Figure 18E-F) proposed a similar approach that they infiltrated perovskite solution into mesoporous silica followed by drying, synthesizing desired perovskite nanoparticles by the confinement of templates.[225,226] Size distributions could be adjusted by the pores of silica to even 3.3 nm without sacrificing the high luminescent efficiency.

4.2 | Applications

4.2.1 | Solar cells

The pioneering work by Mayasiki in 2009 successfully demonstrated a perovskite nanocrystal-based solar cell,

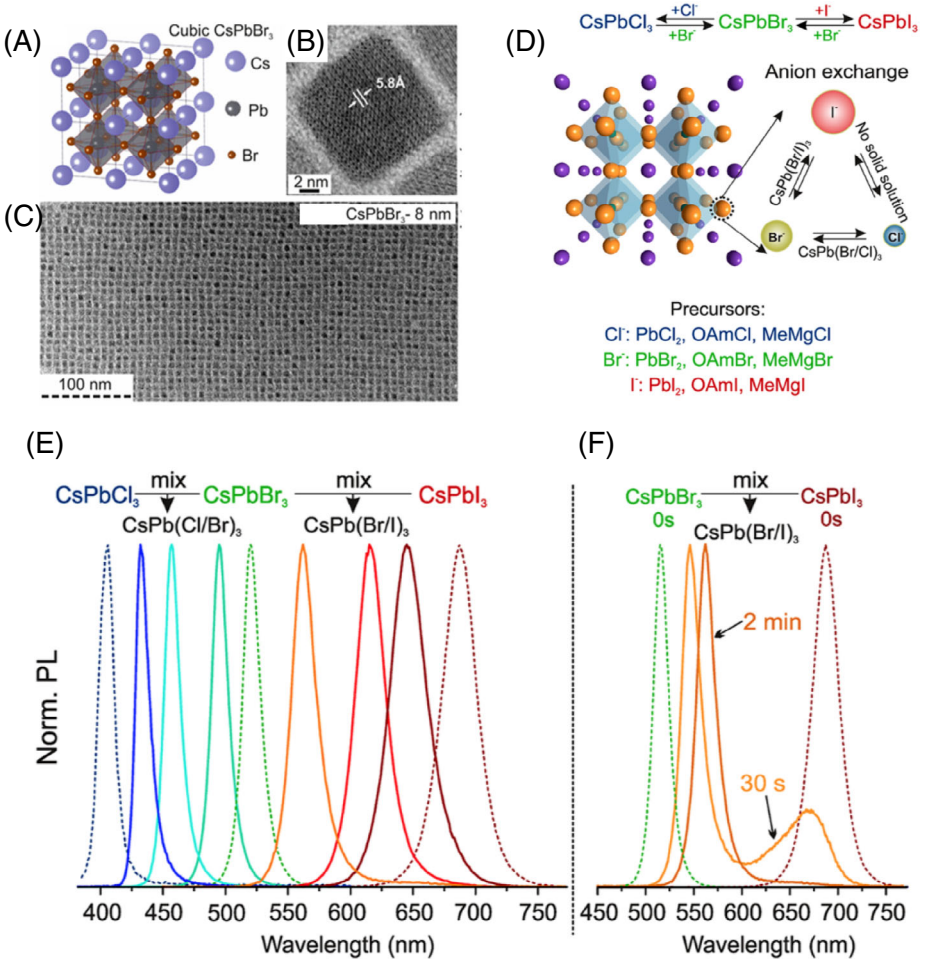

FIGURE 17 A-C, Schematic of the cubic $CsPbBr_3$ structure (A) and transmission electron microscope (TEM) image of $CsPbBr_3$ nanocrystals from the hot-injection method at different magnifications (B-C). Reproduced with permission.[220] Copyright 2015 American Chemical Society. D, Schematic illumination of anion-exchange inside the cubic $CsPbX_3$ structure. The agents listed here are suitable for the anion-exchange reaction. Reproduced with permission. E, Normalized photoluminescence (PL) spectra of $CsPbX_3$ nanocrystals with different compositions obtained from the inter-nanocrystal anion-exchange reactions. F, PL evolutions of $CsPbX_3$ nanocrystals during the inter-nanocrystal anion-exchange reaction. Reproduced with permission.[221] Copyright 2015 American Chemical Society

exhibiting a PCE of 3.8% (Figure 19A).[6] The performance was further improved by the Park group to 6.54% (Figure 19B-E), a record efficiency among perovskite nanocrystal-based PV devices.[16] The research focus then moves onto inorganic counterparts like $CsPbI_3$ quantum dots owing to the consideration of tandem devices.[125,126,128] Swarnkar et al. in 2016 developed a novel process to purify the as-formed quantum dots by the selection of methyl acetate, an antisolvent that removes excess unreacted reagents.[125] The stability was significantly enhanced for the purified sample, which was stable in the cubic phase for months (Figure 19F). Solar cells based on these stable quantum dots showed an impressive PCE exceeding 10%, with a high open-circuit voltage up to 1.23 V. Further investigation, like utilizing AX salts like FAI to tune the coupling between perovskite quantum dots and increase charge transport properties between quantum dots arrays, boosted a record efficiency of quantum dots-based solar cell up to 13.4% (Figure 19H-J).[126] A summary of the performance of perovskite nanocrystal-based solar cells is listed in Table 1.

4.2.2 | LEDs

High binding energy, strong PLQY together with tunable color gamut made perovskite quantum dots rather promising for LED fabrication.[152-154] Song et al. used inorganic $CsPbX_3$ quantum dots as emitters in LEDs for the first time (Figure 20A).[152] It showed a wide color tunability from blue to orange by simply changing the anionic composition, but a low luminance and EQE accompanied simultaneously (Figure 20B). The moderate performance

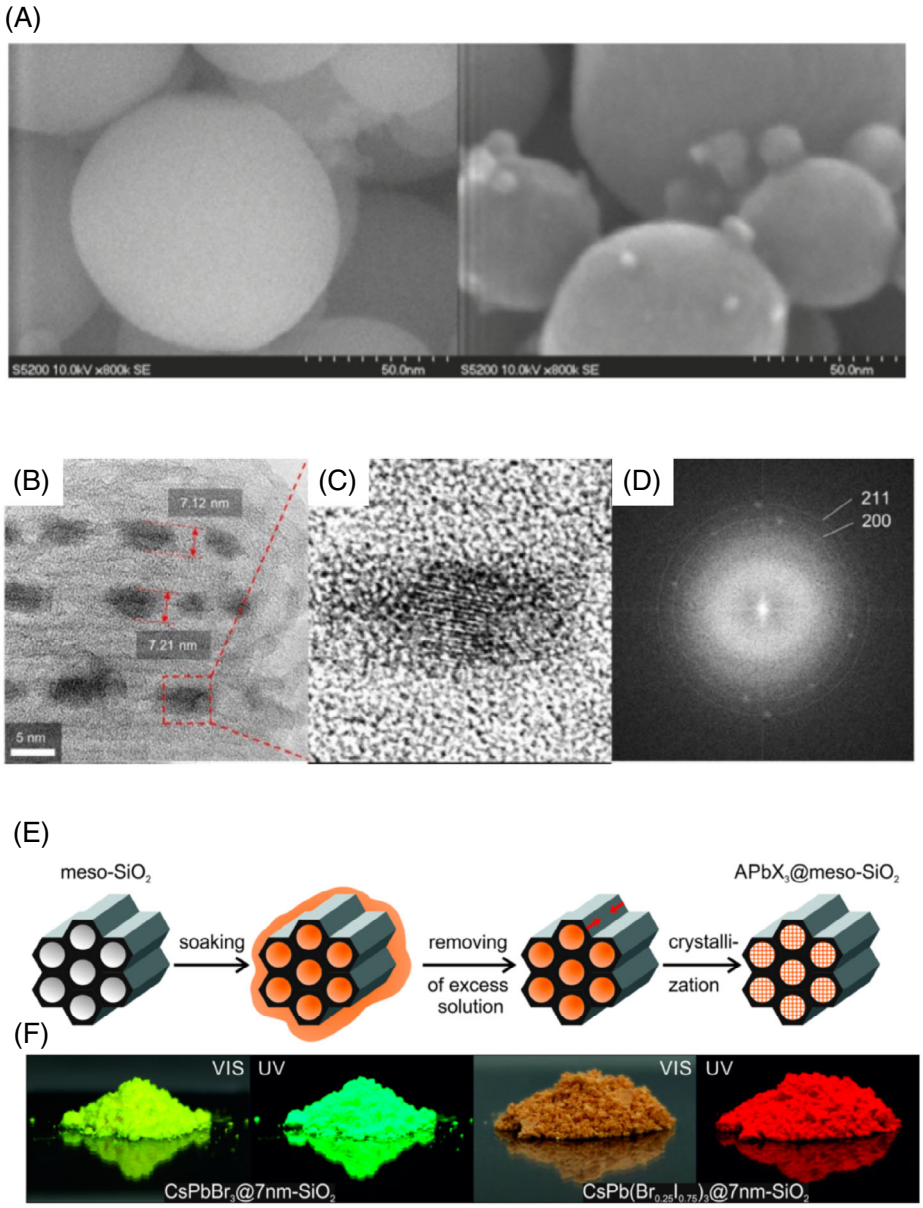

FIGURE 18 A, Scanning electron microscope (SEM) images of bare Al_2O_3 nanoparticles and $MAPbBr_3$ nanoparticles on the Al_2O_3 surface. Reproduced with permission.[224] Copyright 2012 The Chemical Society of Japan. B-D, High-resolution transmission electron microscope (TEM) images of $MAPbBr_xI_{3-x}$ perovskite/silica composites. Reproduced with permission.[225] Copyright 2016 American Chemical Society. E, Schematic of template-assisted synthesis of $APbX_3$ nanocrystals ($A = Cs^+$, MA, FA; $X = Br^-$ or I^-) in the pores of mesoporous silica. F, Photographs of mesoporous silica impregnated with $CsPbX_3$ nanocrystals under daylight and UV light. Reproduced with permission.[226] Copyright 2016 American Chemical Society

is possibly attributed to the excess long ligand on quantum dots' surface that hampered the efficient carrier transporting. Replacing these long ligands with shorter one would address this issue effectively. Pan et al. realized efficient LEDs based on $CsPbX_3$ quantum dots, which were capped by relatively short ligand (eg, didodecyl dimethyl ammonium bromide) (Figure 20C), and achieved much improved EQE (1.9% for the blue, and 3.0% for the green) (Figure 20D-E).[154] Li et al. achieved a 50-fold EQE enhancement by balancing surface passivation and carrier injection of perovskite quantum dots (Figure 20F). An EQE up to 6.27% in the $CsPbBr_3$ nanocrystal-based LED has been obtained by precisely controlling the ligand density on the surface. Besides, the current efficiency was 30-fold improved up to 13.3 cd A^{-1}, as well (Figure 20G).[153] In addition to these solutions, other strategies like surface engineering and so on were also proposed to address the remaining problem,

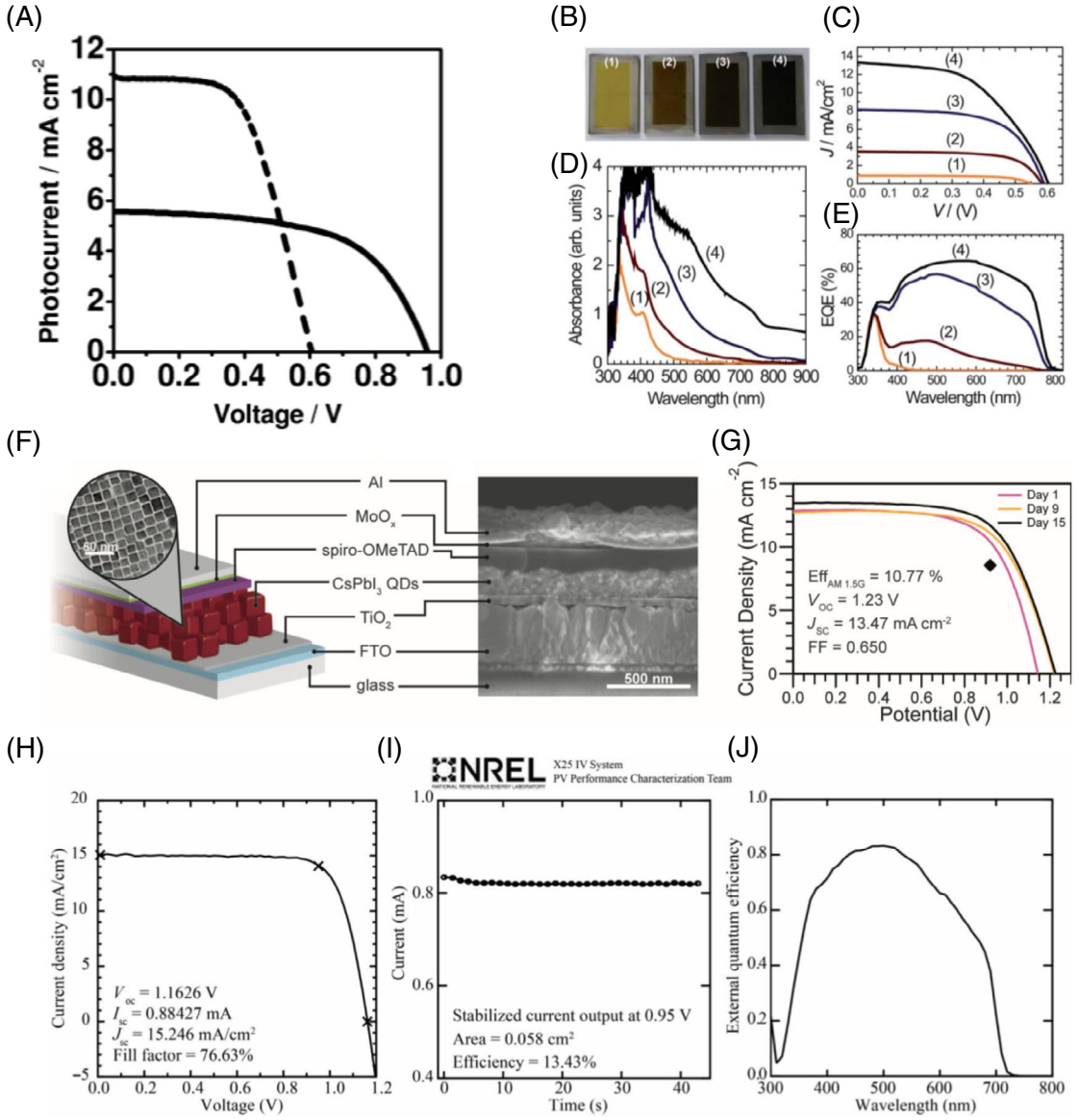

FIGURE 19 A, J-V curves of perovskite solar cells based on $MAPbI_3$ quantum dots (dashed line) and $MAPbBr_3$ quantum dots (solid line). Reproduced with permission.[6] Copyright 2009 American Chemical Society. B, Photographs of $MAPbI_3$ quantum dot-sensitized 5.5 μm thick TiO_2 films fabricated with different precursor concentrations. From left to right the concentrations are 10.05, 20.13, 30.18, and 40.26 wt %. C, J-V curves of solar cells based $MAPbI_3$ quantum dot-sensitized 5.5 μm thick TiO_2 films with different concentrations. D, Absorption spectra of $MAPbI_3$ quantum dot-sensitized 1.4 μm thick TiO_2 films with different concentrations. E, The corresponding external quantum efficiency (EQE) spectra of devices in figure C. Reproduced with permission.[16] Copyright 2011 The Royal Society of Chemistry. F, Device structure of a $CsPbI_3$ quantum dot-based solar cell and a corresponding cross-sectional scanning electron microscope (SEM) image of the device. G, J-V curves of the $CsPbI_3$ quantum dot-based solar cell measured at different times. Reproduced with permission.[125] Copyright 2016 AAAS. H, J-V curves of the $CsPbI_3$ quantum dot-based solar cell with a certified efficiency. I, I-t curve of the corresponding device in figure H, showing a stabilized PCE of 13.43%. J, EQE spectrum of the corresponding device in figure H. Reproduced with permission.[126] Copyright 2017 AAAS

significantly accelerating the development of nanocrystals based LEDs.[150,151,155-158,228,229] Recently, some types of 0D perovskites were demonstrated to possess broadband emission, which are promising candidates for the applications of down-conversion white LEDs.[50,230-233] Zhou et al. replaced the element lead by tin and selected different ligands, demonstrating 0D perovskites with tunable broad emission.[230] Through the manipulation of locally collective hydrogen bonding, Cui et al. successfully tailored the assembling behavior and synthesized 0D perovskite single crystal with "warm" white emission and enhanced PL efficiency.[231] By combining the hybrid

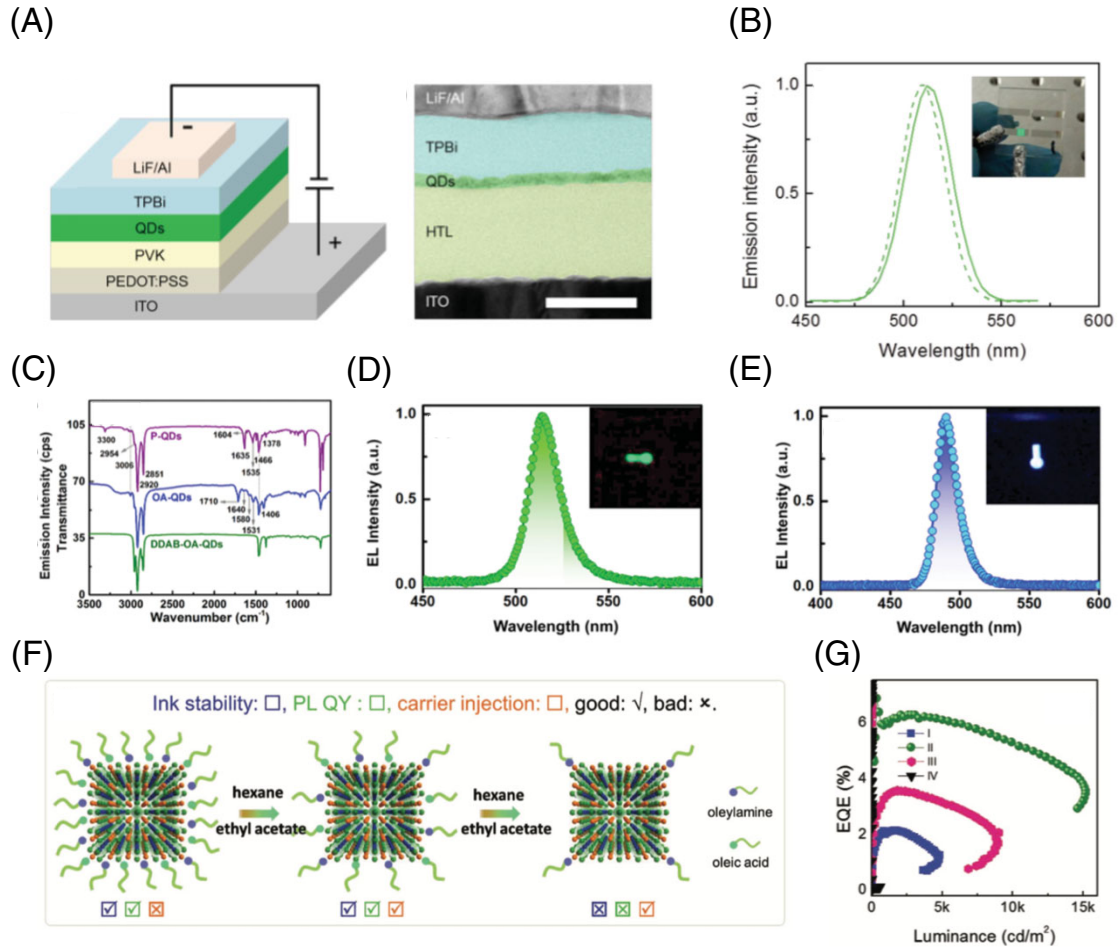

FIGURE 20 A, Schematic of the structure of the $CsPbX_3$ quantum dot-based LED and corresponding cross-sectional scanning electron microscope (SEM) image of the device. B, Electroluminescence (EL) spectrum of the $CsPbBr_3$ quantum dot-based LED measured at a voltage of 5.5 V. The inset is a photograph of a device with an active area of 2×2 mm^2. Reproduced with permission.[152] Copyright 2015 Wiley-VCH. C, Fourier-transform infrared spectroscopy (FTIR) spectra of $CsPbBr_3$ quantum dots with different surface treatments. D, EL spectrum of LEDs based on $CsPbBr_3$ quantum dots. E, EL spectrum of LEDs based on $CsPbBr_xCl_{3-x}$ quantum dots. Insets are photographs of the corresponding devices. Reproduced with permission.[154] Copyright 2016 Wiley-VCH. F, Schematic illustration of the control of ligand density on $CsPbBr_3$ quantum dot surfaces and the corresponding ink stability, photoluminescent quantum yield (PLQY), and carrier injection. G, External quantum efficiency (EQE) spectra of $CsPbBr_3$ quantum dot-based light-emitting diodes (LEDs) as a function of luminance. Reproduced with permission.[153] Copyright 2017 Wiley-VCH

with the commercial phosphor in various ratios, Worku et al. fabricated UV-pumped white LEDs with tunable color gamut, from "cold" to "warm" white.[232] More detailed parameters of LEDs based on perovskite nanocrystals are listed in Table 2.

4.2.3 | Lasers

In 2015, Yakunin demonstrated the spontaneous emission and lasing in blue and green spectral regions from ~10 nm monodispersed $CsPbX_3$ nanocrystals.[234] Low pump thresholds down to 5 ± 1 μJ cm^{-2}, together with high values of a modal net gain of at least 450 ± 30 cm^{-1}, were demonstrated in this system (Figure 21A). Two lasing modes were observed. One was the whispering-gallery-mode where silica microspheres as high-finesse resonators were coated with $CsPbX_3$ nanocrystals and the other was random lasing in films of $CsPbX_3$ nanocrystals. Later work by Wang et al. demonstrated a $CsPbX_3$ nanocrystal-based laser, with a low threshold of 22 μJ cm^{-2}, wide color tunability, and good stability (Figure 21B).[235] Based on this, the same group investigated the manifested nonlinear absorption and multiphoton pumped stimulated emission from 9 nm-sized $CsPbBr_3$ nanocrystals (Figure 21C). Low-threshold and tunable frequency-

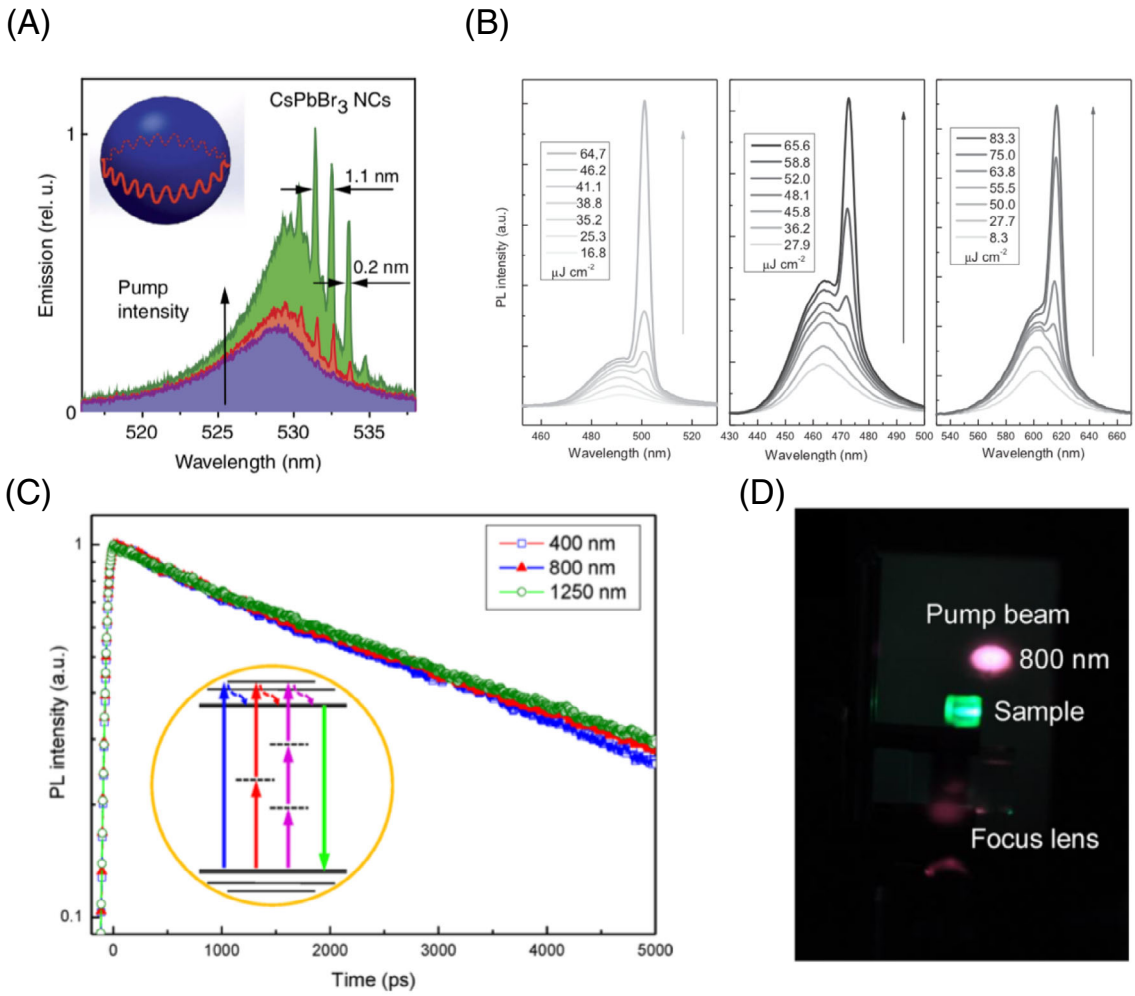

FIGURE 21 A, Photoluminescence (PL) emissions of a microsphere resonator (15 μm in diameter, covered by a film of $CsPbBr_3$ nanocrystals) at the excitation intensities around the lasing threshold. The inset is a schematic of whispering-gallery-mode (WGM) lasing in a sphere. Reproduced with permission.[234] Copyright 2015 Nature Publishing Group. B, Stimulated emission from small-sized $CsPbX_3$ quantum dots with different compositions. Reproduced with permission.[235] Copyright 2015 Wiley-VCH. C, PL decays of $CsPbBr_3$ nanocrystals based on one-, two-, and three-photon excitation. The inset is an illustration of the whole process of one-, two-, and three-photon excited PL. D, Photograph of the stripe pumping configuration. A strong green PL can be seen by the pump of 800 nm laser. Reproduced with permission.[236] Copyright 2016 American Chemical Society

upconverted stimulated emission by two-photon absorption and green stimulated emission by three-photon were both obtained from the $CsPbCl_xBr_{3-x}$ nanocrystals, providing promising opportunities in nonlinear photonics (Figure 21D).[236]

5 | OUTLOOK

Although 3D perovskite has been investigated intensively, the exploration of low-dimensional perovskites has not caught the pace of 3D counterparts in multiple aspects. It can be expected that advantages arising from low dimensionality can be further magnified both fundamentally and practically.

5.1 | Precise control of the size and dimensionality

As one of the most valuable merits with reduced dimensionality, size and dimensional control for various bandgaps attract tremendous attention. Nowadays, although some groups can manipulate the perovskites with size and shape control to some degree, most synthesis methods for low-dimensional perovskites are trial-and-error, without a precise regulation. With the emerging machine learning techniques recently,[237-241] Lu et al. can predict enormous perovskite structures and even material stability, according to the former database.[239] We are inquisitive whether this approach can be utilized as the guidelines for the synthesis of

perovskites with accurate structures and dimensions we desire. Based on these, more explorations of in-depth physical mechanism and wide applications will be duly concomitant.

5.2 | Understanding of the physics in low-dimensional perovskites

Since tremendous optoelectronic applications have been demonstrated, the investigations focusing on fundamental properties of low-dimensional perovskites have not attracted much attention. With the reduced dimensions, some inherent natures like band structure and photon transport will behave differently. For example, reduced thermal conductance from the enhanced boundary scattering, together with the improved Seebeck coefficient from the modified energy band, makes low-dimensional perovskites potential materials for thermoelectrics.[242-246] Recently, Wang et al. have investigated the cation dynamics governed by thermal properties in different types of perovskite nanowires.[244] However, the study on this aspect is limited and more efforts should be devoted to further exploration. In addition, the low dimensionality could also bring about confined charge transport in the selected directions, leading to unique electrical properties such as 2D electron gas, which is the basis for field-effect devices.[247,248] However, these fundamental investigations rather lag behind the application and is supposed to draw more attention in the near future.

5.3 | Exploration of new applications

In addition to the applications in solar cells, LEDs, lasers, and photodetectors, metal halide perovskites may possess other suitable uses. For example, Liao et al. have demonstrated ferroelectricity in bulk 3D perovskite.[249] It is expected that the strong quantum and dielectric confinements of nanostructures may bring up much-enhanced ferroelectricity, which calls for more systematic investigations in low-dimensional nanoplatelets or nanowires.

ACKNOWLEDGMENTS

This work is supported by the National Natural Science Foundation of China (Nos. 21805132, 11574143, 11874211, 11621091, 61735008) and the Natural Science Foundation of Jiangsu Province (No. BK20180341) and the Fundamental Research Funds for the Central Universities (Nos. 021314380128 and 021314380135).

CONFLICT OF INTEREST

The authors declare no potential conflict of interest.

ORCID

Jia Zhu https://orcid.org/0000-0002-2871-4369

REFERENCES

1. Møller C. Crystal structure and photoconductivity of caesium plumbo-halides. *Nature*. 1958;182(4647):1436-1436.
2. Mitzi DB. Synthesis, structure, and properties of organic-inorganic perovskites and related materials. *Prog Inorg Chem*. 1999;48:1-121.
3. Mitzi DB, Feild CA, Harrison WTA, Guloy AM. Conducting tin halides with a layered organic-based perovskite structure. *Nature*. 1994;369(6480):467-469.
4. Weber DZ. $CH_3NH_3SnBr_xI_{3-x}$(x = 0-3), a Sn(II)-system with cubic perovskite structure. *Z Naturforsch*. 1978;33b: 862-865.
5. Kagan CR, Mitzi DB, Dimitrakopoulos CD. Organic-inorganic hybrid materials as semiconducting channels in thin-film field-effect transistors. *Science*. 1999;286(5441):945-947.
6. Kojima A, Teshima K, Shirai Y, Miyasaka T. Organometal halide perovskites as visible-light sensitizers for photovoltaic cells. *J Am Chem Sci*. 2009;131(17):6050-6051.
7. Liang K, Mitzi DB, Prikas MT. Synthesis and characterization of organic-inorganic perovskite thin films prepared using a versatile two-step dipping technique. *Chem Mater*. 1998;10(1): 403-411.
8. Dong Q, Fang Y, Shao Y, et al. Electron-hole diffusion lengths >175 μm in solution-grown $CH_3NH_3PbI_3$ single crystals. *Science*. 2015;347(6225):967-970.
9. Shi D, Adinolfi V, Comin R, et al. Low trap-state density and long carrier diffusion in organolead trihalide perovskite single crystals. *Science*. 2015;347(6221): 519-522.
10. Green MA, Ho-Baillie A, Snaith HJ. The emergence of perovskite solar cells. *Nat Photonics*. 2014;8(7):506-514.
11. Lee MM, Teuscher J, Miyasaka T, Murakami TN, Snaith HJ. Efficient hybrid solar cells based on meso-superstructured organometal halide perovskites. *Science*. 2012;338(6107): 643-647.
12. Park N-G. Perovskite solar cells: an emerging photovoltaic technology. *Mater Today*. 2015;18(2):65-72.
13. Malinkiewicz O, Yella A, Lee YH, et al. Perovskite solar cells employing organic charge-transport layers. *Nat Photonics*. 2013;8(2):128-132.
14. Burschka J, Pellet N, Moon SJ, et al. Sequential deposition as a route to high-performance perovskite-sensitized solar cells. *Nature*. 2013;499(7458):316-319.
15. Tan H, Jain A, Voznyy O, et al. Efficient and stable solution-processed planar perovskite solar cells via contact passivation. *Science*. 2017;355(6326):722-726.
16. Im JH, Lee CR, Lee JW, Park SW, Park NG. 6.5% efficient perovskite quantum-dot-sensitized solar cell. *Nanoscale*. 2011; 3(10):4088-4093.
17. Sutherland BR, Sargent EH. Perovskite photonic sources. *Nat Photonics*. 2016;10(5):295-302.

18. Tan ZK, Moghaddam RS, Lai ML, et al. Bright light-emitting diodes based on organometal halide perovskite. *Nat Nanotechnol*. 2014;9(9):687-692.
19. Cho H, Jeong SH, Park MH, et al. Overcoming the electroluminescence efficiency limitations of perovskite light-emitting diodes. *Science*. 2015;350(6265):1222-1225.
20. Dou L, Yang YM, You J, et al. Solution-processed hybrid perovskite photodetectors with high detectivity. *Nat Commun*. 2014;5:5404.
21. Xing G, Mathews N, Lim SS, et al. Low-temperature solution-processed wavelength-tunable perovskites for lasing. *Nat Mater*. 2014;13(5):476-480.
22. Lee J-W, Kim D-H, Kim H-S, Seo S-W, Cho SM, Park N-G. Formamidinium and cesium hybridization for photo- and moisture-stable perovskite solar cell. *Adv Energy Mater*. 2015;5(20):1501310.
23. Wu Y, Xie F, Chen H, et al. Thermally stable $MAPbI_3$ perovskite solar cells with efficiency of 19.19% and area over 1 cm^2 achieved by additive engineering. *Adv Mater*. 2017;29(28):1701073.
24. Wang Y, Zhang T, Kan M, Li Y, Wang T, Zhao Y. Efficient α-$CsPbI_3$ photovoltaics with surface terminated organic cations. *Joule*. 2018;2(10):2065-2075.
25. Sutton RJ, Eperon GE, Miranda L, et al. Bandgap-tunable cesium lead halide perovskites with high thermal stability for efficient solar cells. *Adv Energy Mater*. 2016;6(8):1502458.
26. Noh JH, Im SH, Heo JH, Mandal TN, Seok SI. Chemical management for colorful, efficient, and stable inorganic-organic hybrid nanostructured solar cells. *Nano Lett*. 2013;13(4):1764-1769.
27. Sadhanala A, Ahmad S, Zhao B, et al. Blue-green color tunable solution processable organolead chloride-bromide mixed halide perovskites for optoelectronic applications. *Nano Lett*. 2015;15(9):6095-6101.
28. Snaith HJ. Perovskites: the emergence of a new era for low-cost, high-efficiency solar cell. *J Phys Chem Lett*. 2013;4(21):3623-3630.
29. Li Z, Yang M, Park JS, et al. Stabilizing perovskite structures by tuning tolerance factor: formation of formamidinium and cesium lead iodide solid-state alloys. *Chem Mater*. 2015;28(1):284-292.
30. Saidaminov MI, Mohammed OF, Bakr OM. Low-dimensional-networked metal halide perovskites: the next big thing. *ACS Energy Lett*. 2017;2(4):889-896.
31. Lu P, Lu M, Wang H, et al. Metal halide perovskite nanocrystals and their applications in optoelectronic devices. *InfoMat*. 2019;1:430-459.
32. Leijtens T, Eperon GE, Noel NK, Habisreutinger SN, Petrozza A, Snaith HJ. Stability of metal halide perovskite solar cells. *Adv Energy Mater*. 2015;5(20):1500963.
33. Li C, Lu X, Ding W, Feng L, Gao Y, Guo Z. Formability of ABX_3 (X = F, Cl, Br, I) halide perovskites. *Acta Crystallogr B*. 2008;64(6):702-707.
34. Lee JW, Seol DJ, Cho AN, Park NG. High-efficiency perovskite solar cells based on the black polymorph of $HC(NH_2)_2PbI_3$. *Adv Mater*. 2014;26(29):4991-4998.
35. Cheng Z, Lin J. Layered organic-inorganic hybrid perovskites: structure, optical properties, film preparation, patterning and templating engineering. *CrystEngComm*. 2010;12(10):2646-2662.
36. Giorgi G, Fujisawa JI, Segawa H, Yamashita K. Organic-inorganic hybrid lead iodide perovskite featuring zero dipole moment guanidinium cations: a theoretical analysis. *J Phys Chem C*. 2015;119(9):4694-4701.
37. Chen J, Kim SG. Park NG. $FA_{0.88}Cs_{0.12}PbI_{3-x}(PF_6)_x$ interlayer formed by ion exchange reaction between perovskite and hole transporting layer for improving photovoltaic performance and stability. *Adv Mater*. 2018;30(40):1801948.
38. Lin J, Lai M, Dou L, et al. Thermochromic halide perovskite solar cells. *Nat Mater*. 2018;17(3):261-267.
39. Wang Y, Dar MI, Ono LK, et al. Thermodynamically stabilized β-$CsPbI_3$-based perovskite solar cells with efficiencies >18%. *Science*. 2019;365(6453):591-595.
40. Eperon GE, Stranks SD, Menelaou C, Johnston MB, Herz LM, Snaith HJ. Formamidinium lead trihalide: a broadly tunable perovskite for efficient planar heterojunction solar cells. *Energy Environ Sci*. 2014;7(3):982-988.
41. Hong K, Van Le Q, Kim SY, et al. Low-dimensional halide perovskites: review and issues. *J Mater Chem C*. 2018;6(9):2189-2209.
42. Zhang Y, Liu J, Wang Z, et al. Synthesis, properties, and optical applications of low-dimensional perovskites. *Chem Commun*. 2016;52(94):13637-13655.
43. Yusoff ARM, Nazeeruddin MK. Low-dimensional perovskites: from synthesis to stability in perovskite solar cells. *Adv Energy Mater*. 2018;8(26):1702073.
44. Zhou C, Lin H, He Q, et al. Low dimensional metal halide perovskites and hybrids. *Mater Sci Eng R*. 2019;137:38-65.
45. Lin H, Zhou C, Tian Y, Siegrist T, Ma B. Low-dimensional organometal halide perovskites. *ACS Energy Lett*. 2017;3(1):54-62.
46. Shi E, Gao Y, Finkenauer BP, Akriti CAH, Dou L. Two-dimensional halide perovskite nanomaterials and heterostructures. *Chem Soc Rev*. 2018;47(16):6046-6072.
47. Misra RK, Cohen BE, Iagher L, Etgar L. Low-dimensional organic-inorganic halide perovskite: structure, properties, and applications. *ChemSusChem*. 2017;10(19):3712-3721.
48. González-Carrero S, Galian RE, Pérez-Prieto J. Organometal halide perovskites: bulk low-dimension materials and nanoparticles. *Part Part Syst Char*. 2015;32(7):709-720.
49. Yuan Z, Zhou C, Tian Y, et al. One-dimensional organic lead halide perovskites with efficient bluish white-light emission. *Nat Commun*. 2017;8:14051.
50. Zhou C, Tian Y, Wang M, et al. Low-dimensional organic tin bromide perovskites and their photoinduced structural transformation. *Angew Chem Int Ed*. 2017;56(31):9018-9022.
51. Huang J, Lai M, Lin J, Yang P. Rich chemistry in inorganic halide perovskite nanostructures. *Adv Mater*. 2018;30(48):e1802856.
52. Fu Y, Zhu H, Chen J, Hautzinger MP, Zhu XY, Jin S. Metal halide perovskite nanostructures for optoelectronic applications and the study of physical properties. *Nat Rev Mater*. 2019;4(3):169-188.
53. Huo C, Cai B, Yuan Z, Ma B, Zeng H. Two-dimensional metal halide perovskites: theory, synthesis, and optoelectronics. *Small Methods*. 2017;1(3):1600018.
54. Feng J, Gong C, Gao H, et al. Single-crystalline layered metal-halide perovskite nanowires for ultrasensitive photodetectors. *Nat Electron*. 2018;1(7):404-410.

55. Saparov B, Mitzi DB. Organic-inorganic perovskites: structural versatility for functional materials design. *Chem Rev*. 2016;116(7):4558-4596.
56. Kamminga ME, Fang H-H, Filip MR, et al. Confinement effects in low-dimensional lead iodide perovskite hybrids. *Chem Mater*. 2016;28(13):4554-4562.
57. Gao P, Bin Mohd Yusoff AR, Nazeeruddin MK. Dimensionality engineering of hybrid halide perovskite light absorbers. *Nat Commun*. 2018;9(1):5028.
58. Grancini G, Nazeeruddin MK. Dimensional tailoring of hybrid perovskites for photovoltaics. *Nat Rev Mater*. 2018;4(1):4-22.
59. Koh TM, Shanmugam V, Schlipf J, et al. Nanostructuring mixed-dimensional perovskites: a route toward tunable, efficient photovoltaics. *Adv Mater*. 2016;28(19):3653-3661.
60. Sichert JA, Tong Y, Mutz N, et al. Quantum size effect in organometal halide perovskite nanoplatelets. *Nano Lett*. 2015;15(10):6521-6527.
61. Hintermayr VA, Richter AF, Ehrat F, et al. Tuning the optical properties of perovskite nanoplatelets through composition and thickness by ligand-assisted exfoliation. *Adv Mater*. 2016;28(43):9478-9485.
62. La-Placa MG, Longo G, Babaei A, Martinez-Sarti L, Sessolo M, Bolink HJ. Photoluminescence quantum yield exceeding 80% in low dimensional perovskite thin-films via passivation control. *Chem Commun*. 2017;53(62):8707-8710.
63. Quan LN, Garcia de Arquer FP, Sabatini RP, Sargent EH. Perovskites for light emission. *Adv Mater*. 2018;30(45):e1801996.
64. Zhao L, Rolston N, Lee KM, et al. Influence of bulky organoammonium halide additive choice on the flexibility and efficiency of perovskite light-emitting devices. *Adv Funct Mater*. 2018;28(31):1802060.
65. Saidaminov MI, Almutlaq J, Sarmah S, et al. Pure Cs_4PbBr_6: highly luminescent zero-dimensional perovskite solids. *ACS Energy Lett*. 2016;1(4):840-845.
66. Gao Y, Zhao L, Shang Q, et al. Ultrathin $CsPbX_3$ nanowire arrays with strong emission anisotropy. *Adv Mater*. 2018;30(31):e1801805.
67. Zhao X, Hao H, Dong J, et al. Fast extraction of electron across the interface of nanowire $CH_3NH_3PbI_3$/ZnO on flexible PET substrate. *Mater Lett*. 2017;197:139-142.
68. Deng W, Zhang X, Huang L, et al. Aligned single-crystalline perovskite microwire arrays for high-performance flexible image sensors with long-term stability. *Adv Mater*. 2016;28(11):2201-2208.
69. Jeong CK, Baek C, Kingon AI, Park KI, Kim SH. Lead-free perovskite nanowire-employed piezopolymer for highly efficient flexible nanocomposite energy harvester. *Small*. 2018;14(19):e1704022.
70. Zhu B-S, He Z, Yao J-S, et al. Potassium ion assisted synthesis of organic-inorganic hybrid perovskite nanobelts for stable and flexible photodetectors. *Adv Opt Mater*. 2018;6(3):1701029.
71. Yang Z, Wang M, Qiu H, et al. Engineering the exciton dissociation in quantum-confined 2D $CsPbBr_3$ nanosheet films. *Adv Funct Mater*. 2018;28(14):1705908.
72. Milot RL, Sutton RJ, Eperon GE, et al. Charge-carrier dynamics in 2D hybrid metal-halide perovskites. *Nano Lett*. 2016;16(11):7001-7007.
73. Chen Y, Yu S, Sun Y, Liang Z. Phase engineering in Quasi-2D Ruddlesden-Popper perovskites. *J Phys Chem Lett*. 2018;9(10):2627-2631.
74. Dong R, Lan C, Xu X, et al. Novel series of quasi-2D Ruddlesden-Popper perovskites based on short-chained spacer cation for enhanced photodetection. *ACS Appl Mater Interface*. 2018;10(22):19019-19026.
75. Ha ST, Liu X, Zhang Q, Giovanni D, Sum TC, Xiong Q. Synthesis of organic-inorganic lead halide perovskite nanoplatelets: towards high-performance perovskite solar cells and optoelectronic devices. *Adv Opt Mater*. 2014;2(9):838-844.
76. Niu L, Zeng Q, Shi J, et al. Controlled growth and reliable thickness-dependent properties of organic-inorganic perovskite platelet crystal. *Adv Funct Mater*. 2016;26(29):5263-5270.
77. Lan C, Dong R, Zhou Z, et al. Large-scale synthesis of freestanding layer-structured PbI_2 and $MAPbI_3$ nanosheets for high-performance photodetection. *Adv Mater*. 2017;29(39):1702759.
78. Liu J, Xue Y, Wang Z, et al. Two-dimensional $CH_3NH_3PbI_3$ perovskite: synthesis and optoelectronic application. *ACS Nano*. 2016;10(3):3536-3542.
79. Wang G, Li D, Cheng HC, et al. Wafer-scale growth of large arrays of perovskite microplate crystals for functional electronics and optoelectronics. *Sci Adv*. 2015;1(9):e1500613.
80. Niu W, Eiden A, Vijaya Prakash G, Baumberg JJ. Exfoliation of self-assembled 2D organic-inorganic perovskite semiconductors. *Appl Phys Lett*. 2014;104(17):171111.
81. Tian H, Zhao L, Wang X, et al. Extremely low operating current resistive memory based on exfoliated 2D perovskite single crystals for neuromorphic computing. *ACS Nano*. 2017;11(12):12247-12256.
82. Guo Z, Wu X, Zhu T, Zhu X, Huang L. Electron-phonon scattering in atomically thin 2D perovskites. *ACS Nano*. 2016;10(11):9992-9998.
83. Dou L, Wong AB, Yu Y, et al. Atomically thin two-dimensional organic-inorganic hybrid perovskites. *Science*. 2015;349(6255):1518-1521.
84. Chen J, Gan L, Zhuge F, et al. A ternary solvent method for large-sized two-dimensional perovskites. *Angew Chem Int Ed*. 2017;56(9):2390-2394.
85. Nordell KJ, Boatman EM, Lisensky GC. A safer, easier, faster synthesis for CdSe quantum dot nanocrystals. *J Chem Educ*. 2005;82(11):1697.
86. Dabbousi BO, Rodriguez-Viejo J, Mikulec FV, et al. (CdSe) ZnS core-shell quantum dots: synthesis and characterization of a size series of highly luminescent nanocrystallites. *J Phys Chem B*. 1997;101(46):9463-9475.
87. Peng X, Manna L, Yang W, et al. Shape control of CdSe nanocrystals. *Nature*. 2000;404(6773):59-61.
88. Danek M, Jensen KF, Murray CB, Bawendi MG. Synthesis of luminescent thin-film CdSe/ZnSe quantum dot composites using CdSe quantum dots passivated with an overlayer of ZnSe. *Chem Mater*. 1996;8(1):173-180.
89. Tyagi P, Arveson SM, Tisdale WA. Colloidal Organohalide perovskite nanoplatelets exhibiting quantum confinement. *J Phys Chem Lett*. 2015;6(10):1911-1916.
90. Bekenstein Y, Koscher BA, Eaton SW, Yang P, Alivisatos AP. Highly luminescent colloidal nanoplates of perovskite cesium

lead halide and their oriented assemblies. *J Am Chem Soc*. 2015;137(51):16008-16011.
91. Akkerman QA, Motti SG, Srimath Kandada AR, et al. Solution synthesis approach to colloidal cesium lead halide perovskite nanoplatelets with monolayer-level thickness control. *J Am Chem Soc*. 2016;138(3):1010-1016.
92. Shamsi J, Dang Z, Bianchini P, et al. Colloidal synthesis of quantum confined single crystal $CsPbBr_3$ nanosheets with lateral size control up to the micrometer range. *J Am Chem Soc*. 2016;138(23):7240-7243.
93. Smith IC, Hoke ET, Solis-Ibarra D, McGehee MD, Karunadasa HI. A layered hybrid perovskite solar-cell absorber with enhanced moisture stability. *Angew Chem Int Ed*. 2014;53(42):11232-11235.
94. Cao DH, Stoumpos CC, Farha OK, Hupp JT, Kanatzidis MG. 2D homologous perovskites as light-absorbing materials for solar cell applications. *J Am Chem Soc*. 2015;137(24):7843-7850.
95. Niu G, Guo X, Wang L. Review of recent progress in chemical stability of perovskite solar cells. *J Mater Chem A*. 2015;3(17):8970-8980.
96. Li P, Chen Y, Yang T, et al. Two-dimensional $CH_3NH_3PbI_3$ perovskite nanosheets for ultrafast pulsed fiber lasers. *ACS Appl Mater Interface*. 2017;9(14):12759-12765.
97. Li R, Yi C, Ge R, et al. Room-temperature electroluminescence from two-dimensional lead halide perovskites. *Appl Phys Lett*. 2016;109(15):151101.
98. Tsai H, Nie W, Blancon JC, et al. High-efficiency two-dimensional Ruddlesden-Popper perovskite solar cells. *Nature*. 2016;536(7616):312-316.
99. Quan LN, Yuan M, Comin R, et al. Ligand-stabilized reduced-dimensionality perovskites. *J Am Chem Soc*. 2016;138(8):2649-2655.
100. Fu W, Wang J, Zuo L, et al. Two-dimensional perovskite solar cells with 14.1% power conversion efficiency and 0.68% external radiative efficiency. *ACS Energy Lett*. 2018;3(9):2086-2093.
101. Gao L, Zhang F, Xiao C, et al. Improving charge transport via intermediate-controlled crystal growth in 2D perovskite solar cells. *Adv Funct Mater*. 2019;1:901652.
102. Chen Y, Sun Y, Peng J, et al. Tailoring organic cation of 2D air-stable organometal halide perovskites for highly efficient planar solar cells. *Adv Energy Mater*. 2017;7(18):1700162.
103. Yang R, Li R, Cao Y, et al. Oriented quasi-2D perovskites for high performance optoelectronic devices. *Adv Mater*. 2018;30(51):1804771.
104. Zhang X, Wu G, Yang S, et al. Vertically oriented 2D layered perovskite solar cells with enhanced efficiency and good stability. *Small*. 2017;13(33):1700611.
105. Zuo C, Scully AD, Vak D, et al. Self-assembled 2D perovskite layers for efficient printable solar cells. *Adv Energy Mater*. 2019;9(4):1803258.
106. Wu G, Li X, Zhou J, et al. Fine multi-phase alignments in 2D perovskite solar cells with efficiency over 17% via slow post-annealing. *Adv Mater*. 2019;31(42):1903889.
107. Soe CMM, Nie W, Stoumpos CC, et al. Understanding film formation morphology and orientation in high member 2D Ruddlesden-Popper perovskites for high-efficiency solar cells. *Adv Energy Mater*. 2018;8(1):1700979.
108. Zhou N, Shen Y, Li L, et al. Exploration of crystallization kinetics in quasi two-dimensional perovskite and high performance solar cells. *J Am Chem Soc*. 2017;140(1):459-465.
109. Zhang X, Ren X, Liu B, et al. Stable high efficiency two-dimensional perovskite solar cells via cesium doping. *Energy Environ Sci*. 2017;10(10):2095-2102.
110. Tan S, Zhou N, Chen Y, et al. Effect of high dipole moment cation on layered 2D organic-inorganic halide perovskite solar cells. *Adv Energy Mater*. 2019;9(5):1803024.
111. Li N, Zhu Z, Chueh CC, et al. Mixed cation $FA_xPEA_{1-x}PbI_3$ with enhanced phase and ambient stability toward high-performance perovskite solar cells. *Adv Energy Mater*. 2017;7(1):1601307.
112. Li MH, Yeh HH, Chiang YH, et al. Highly efficient 2D/3D hybrid perovskite solar cells via low-pressure vapor-assisted solution process. *Adv Mater*. 2018;30(30):1801401.
113. Wang Z, Lin Q, Chmiel FP, Sakai N, Herz LM, Snaith HJ. Efficient ambient-air-stable solar cells with 2D-3D heterostructured butylammonium-caesium-formamidinium lead halide perovskites. *Nat Energy*. 2017;2(9):17135.
114. Li P, Zhang Y, Liang C, et al. Phase pure 2D perovskite for high-performance 2D-3D Heterostructured perovskite solar cells. *Adv Mater*. 2018;30(52):1805323.
115. Zhou T, Lai H, Liu T, et al. Highly efficient and stable solar cells based on crystalline oriented 2D/3D hybrid perovskite. *Adv Mater*. 2019;31(32):1901242.
116. Im JH, Luo J, Franckevicius M, et al. Nanowire perovskite solar cell. *Nano Lett*. 2015;15(3):2120-2126.
117. Chang C-Y, Tsai B-C, Lin M-Z, Huang Y-C, Tsao C-S. An integrated approach towards the fabrication of highly efficient and long-term stable perovskite nanowire solar cells. *J Mater Chem A*. 2017;5(43):22824-22 833.
118. Singh R, Suranagi SR, Yang SJ, Cho K. Enhancing the power conversion efficiency of perovskite solar cells via the controlled growth of perovskite nanowires. *Nano Energy*. 2018;51:192-198.
119. Wang S, Yan S, Wang M, Chang L, Wang J, Wang Z. Construction of nanowire $CH_3NH_3PbI_3$-based solar cells with 17.62% efficiency by solvent etching technique. *Sol Energy Mater Sol Cells*. 2017;167:173-177.
120. Liao J-F, Li W-G, Rao H-S, et al. Inorganic cesium lead halide $CsPbX_3$ nanowires for long-term stable solar cells. *Sci China Mater*. 2017;60(4):285-294.
121. Chen LJ, Lee CR, Chuang YJ, Wu ZH, Chen C. Synthesis and optical properties of Lead-free cesium tin halide perovskite quantum rods with high-performance solar cell application. *J Phys Chem Lett*. 2016;7(24):5028-5035.
122. Mali SS, Shim CS, Hong CK. Highly stable and efficient solid-state solar cells based on methylammonium lead bromide ($CH_3NH_3PbBr_3$) perovskite quantum dots. *NPG Asia Mater*. 2015;7(8):e208.
123. Xue J, Lee JW, Dai Z, et al. Surface ligand management for stable $FAPbI_3$ perovskite quantum dot solar cells. *Joule*. 2018;2(9):1866-1878.
124. Xue J, Wang R, Chen L, et al. A small-molecule "charge driver" enables perovskite quantum dot solar cells with efficiency approaching 13%. *Adv Mater*. 2019;31(27):1900111.

125. Swarnkar A, Marshall AR, Sanehira EM, et al. Quantum dot-induced phase stabilization of α-$CsPbI_3$ perovskite for high-efficiency photovoltaics. *Science*. 2016;354(6308):92-95.
126. Sanehira EM, Marshall AR, Christians JA, et al. Enhanced mobility $CsPbI_3$ quantum dot arrays for record-efficiency, high-voltage photovoltaic cells. *Sci Adv*. 2017;3(10): eaao4204.
127. Wang Q, Jin Z, Chen D, et al. μ-Graphene crosslinked $CsPbI_3$ quantum dots for high efficiency solar cells with much improved stability. *Adv Energy Mater*. 2018;8(22):1800007.
128. Yuan J, Ling X, Yang D, et al. Band-aligned polymeric hole transport materials for extremely low energy loss α-$CsPbI_3$ perovskite nanocrystal solar cells. *Joule*. 2018;2(11):2450-2463.
129. Zhao Q, Hazarika A, Chen X, et al. High efficiency perovskite quantum dot solar cells with charge separating heterostructure. *Nat Commun*. 2019;10(1):1-8.
130. Li F, Zhou S, Yuan J, et al. Perovskite quantum dot solar cells with 15.6% efficiency and improved stability enabled by an α-$CsPbI_3$/$FAPbI_3$ bilayer structure. *ACS Energy Lett*. 2019;4 (11):2571-2578.
131. Era M, Morimoto S, Tsutsui T, Saito S. Organic-inorganic heterostructure electroluminescent device using a layered perovskite semiconductor $(C_6H_5C_2H_4NH_3)_2PbI_4$. *Appl Phys Lett*. 1994;65(6):676-678.
132. Liang D, Peng Y, Fu Y, et al. Color-pure violet-light-emitting diodes based on layered Lead halide perovskite nanoplates. *ACS Nano*. 2016;10(7):6897-6904.
133. Byun J, Cho H, Wolf C, et al. Efficient visible quasi-2D perovskite light-emitting diodes. *Adv Mater*. 2016;28(34): 7515-7520.
134. Yuan M, Quan LN, Comin R, et al. Perovskite energy funnels for efficient light-emitting diodes. *Nat Nanotechnol*. 2016;11 (10):872-877.
135. Wang N, Cheng L, Ge R, et al. Perovskite light-emitting diodes based on solution-processed self-organized multiple quantum wells. *Nat Photonics*. 2016;10(11):699-704.
136. Jiang Y, Qin C, Cui M, et al. Spectra stable blue perovskite light-emitting diodes. *Nat Commun*. 2019;10(1):1868.
137. Wu C, Wu T, Yang Y, et al. Alternative type two-dimensional-three-dimensional lead halide perovskite with inorganic sodium ions as a spacer for high-performance light-emitting diodes. *ACS Nano*. 2019;13(2):1645-1654.
138. Zhao B, Bai S, Kim V, et al. High-efficiency perovskite-polymer bulk heterostructure light-emitting diodes. *Nat Photonics*. 2018;12(12):783-789.
139. Chen P, Meng Y, Ahmadi M, et al. Charge-transfer versus energy-transfer in quasi-2D perovskite light-emitting diodes. *Nano Energy*. 2018;50:615-622.
140. Yang X, Zhang X, Deng J, et al. Efficient green light-emitting diodes based on quasi-two-dimensional composition and phase engineered perovskite with surface passivation. *Nat Commun*. 2018;9(1):570.
141. Xiao Z, Kerner RA, Zhao L, et al. Efficient perovskite light-emitting diodes featuring nanometre-sized crystallites. *Nat Photonics*. 2017;11(2):108-115.
142. Ling Y, Yuan Z, Tian Y, et al. Bright light-emitting diodes based on organometal halide perovskite nanoplatelets. *Adv Mater*. 2016;28(2):305-311.
143. Tsai H, Nie W, Blancon JC, et al. Stable light-emitting diodes using phase-pure Ruddlesden-Popper layered perovskites. *Adv Mater*. 2018;30(6):1704217.
144. Yang X, Chu Z, Meng J, et al. Effects of organic cations on the structure and performance of quasi-two-dimensional perovskite-based light-emitting diodes. *J Phys Chem Lett*. 2019;10:2892-2897.
145. Tian Y, Zhou C, Worku M, et al. Highly efficient spectrally stable red perovskite light-emitting diodes. *Adv Mater*. 2018;30 (20):1707093.
146. Zhang S, Yi C, Wang N, et al. Efficient red perovskite light-emitting diodes based on solution-processed multiple quantum wells. *Adv Mater*. 2017;29(22):1606600.
147. Li Z, Chen Z, Yang Y, Xue Q, Yip HL, Cao Y. Modulation of recombination zone position for quasi-two-dimensional blue perovskite light-emitting diodes with efficiency exceeding 5%. *Nat Commun*. 2019;10(1):1027.
148. Deng W, Jin X, Lv Y, Zhang X, Zhang X, Jie J. 2D Ruddlesden-Popper perovskite nanoplate based deep-blue light-emitting diodes for light communication. *Adv Funct Mater*. 2019;29(40):1903861.
149. Wong AB, Lai M, Eaton SW, et al. Growth and anion exchange conversion of $CH_3NH_3PbI_3$ nanorod arrays for light-emitting diodes. *Nano Lett*. 2015;15(8):5519-5524.
150. Li YF, Chou SY, Huang P, et al. Stretchable organometal-halide-perovskite quantum-dot light-emitting diodes. *Adv Mater*. 2019;1:807516.
151. Zhang X, Liu H, Wang W, et al. Hybrid perovskite light-emitting diodes based on perovskite nanocrystals with organic-inorganic mixed cations. *Adv Mater*. 2017;29(18): 1606405.
152. Song J, Li J, Li X, Xu L, Dong Y, Zeng H. Quantum dot light-emitting diodes based on inorganic perovskite cesium lead halides ($CsPbX_3$). *Adv Mater*. 2015;27(44):7162-7167.
153. Li J, Xu L, Wang T, et al. 50-fold EQE improvement up to 6.27% of solution-processed all-inorganic perovskite $CsPbBr_3$ QLEDs via surface ligand density control. *Adv Mater*. 2017;29 (5):1603885.
154. Pan J, Quan LN, Zhao Y, et al. Highly efficient perovskite-quantum-dot light-emitting diodes by surface engineering. *Adv Mater*. 2016;28(39):8718-8725.
155. Yassitepe E, Yang Z, Voznyy O, et al. Amine-free synthesis of cesium lead halide perovskite quantum dots for efficient light-emitting diodes. *Adv Funct Mater*. 2016;26(47):8757-8763.
156. Song J, Fang T, Li J, et al. Organic-inorganic hybrid passivation enables perovskite QLEDs with an EQE of 16.48%. *Adv Mater*. 2018;30(50):1805409.
157. Chiba T, Hayashi Y, Ebe H, et al. Anion-exchange red perovskite quantum dots with ammonium iodine salts for highly efficient light-emitting devices. *Nat Photonics*. 2018;12(11): 681-687.
158. Li G, Rivarola FWR, Davis NJLK, et al. Highly efficient perovskite nanocrystal light-emitting diodes enabled by a universal crosslinking method. *Adv Mater*. 2016;28(18):3528-3534.
159. Veldhuis SA, Boix PP, Yantara N, et al. Perovskite materials for light-emitting diodes and lasers. *Adv Mater*. 2016;28(32): 6804-6834.

160. Tan Z, Wu Y, Hong H, et al. Two-dimensional $(C_4H_9NH_3)_2PbBr_4$ perovskite crystals for high-performance photodetector. *J Am Chem Soc.* 2016;138(51):16612-16615.
161. Song J, Xu L, Li J, et al. Monolayer and few-layer all-inorganic perovskites as a new family of two-dimensional semiconductors for printable optoelectronic devices. *Adv Mater.* 2016;28(24):4861-4869.
162. Li X, Yu D, Chen J, et al. Constructing fast carrier tracks into flexible perovskite photodetectors to greatly improve responsivity. *ACS Nano.* 2017;11(2):2015-2023.
163. Liu X, Yu D, Cao F, et al. Low-voltage photodetectors with high responsivity based on solution-processed micrometer-scale all-inorganic perovskite nanoplatelets. *Small.* 2017;13(25):1700364.
164. Li L, Sun Z, Wang P, et al. Tailored engineering of an unusual $(C_4H_9NH_3)_2$ $(CH_3NH_3)_2Pb_3Br_{10}$ two-dimensional multilayered perovskite ferroelectric for a high-performance photodetector. *Angew Chem Int Ed.* 2017;56(40):12150-12 154.
165. Zhang Y, Liu Y, Xu Z, et al. Two-dimensional $(PEA)_2PbBr_4$ perovskite single crystals for a high performance UV-detector. *J Mater Chem C.* 2019;7(6):1584-1591.
166. Gao L, Zeng K, Guo J, et al. Passivated single-crystalline $CH_3NH_3PbI_3$ nanowire photodetector with high detectivity and polarization sensitivity. *Nano Lett.* 2016;16(12):7446-7454.
167. Zhu P, Gu S, Shen X, et al. Direct conversion of perovskite thin films into nanowires with kinetic control for flexible optoelectronic devices. *Nano Lett.* 2016;16(2):871-876.
168. Horvath E, Spina M, Szekrenyes Z, et al. Nanowires of methylammonium lead iodide $(CH_3NH_3PbI_3)$ prepared by low temperature solution-mediated crystallization. *Nano Lett.* 2014;14(12):6761-6766.
169. Deng W, Huang L, Xu X, et al. Ultrahigh-responsivity photodetectors from perovskite nanowire arrays for sequentially tunable spectral measurement. *Nano Lett.* 2017;17(4):2482-2489.
170. Deng H, Dong D, Qiao K, et al. Growth, patterning and alignment of organolead iodide perovskite nanowires for optoelectronic devices. *Nanoscale.* 2015;7(9):4163-4170.
171. Gu L, Tavakoli MM, Zhang D, et al. 3D arrays of 1024-pixel image sensors based on lead halide perovskite nanowires. *Adv Mater.* 2016;28(44):9713-9721.
172. Shoaib M, Zhang X, Wang X, et al. Directional growth of ultralong $CsPbBr_3$ perovskite nanowires for high-performance photodetectors. *J Am Chem Soc.* 2017;139(44):15592-15595.
173. Chen J, Fu Y, Samad L, et al. Vapor-phase epitaxial growth of aligned nanowire networks of cesium lead halide perovskites ($CsPbX_3$, X = cl, Br, I). *Nano Lett.* 2016;17(1):460-466.
174. Xing J, Liu XF, Zhang Q, et al. Vapor phase synthesis of organometal halide perovskite nanowires for tunable room-temperature nanolasers. *Nano Lett.* 2015;15(7):4571-4577.
175. Zhang W, Peng L, Liu J, et al. Controlling the cavity structures of two-photon-pumped perovskite microlasers. *Adv Mater.* 2016;28(21):4040-4046.
176. Zhang Q, Ha ST, Liu X, Sum TC, Xiong Q. Room-temperature near-infrared high-Q perovskite whispering-gallery planar nanolasers. *Nano Lett.* 2014;14(10):5995-6001.
177. Feng J, Yan X, Zhang Y, et al. "Liquid knife" to fabricate patterning single-crystalline perovskite microplates toward high-performance laser arrays. *Adv Mater.* 2016;28(19):3732-3741.
178. Liao Q, Hu K, Zhang H, Wang X, Yao J, Fu H. Perovskite microdisk microlasers self-assembled from solution. *Adv Mater.* 2015;27(22):3405-3410.
179. Zhang Q, Su R, Liu X, Xing J, Sum TC, Xiong Q. High-quality whispering-gallery-mode lasing from cesium lead halide perovskite nanoplatelets. *Adv Funct Mater.* 2016;26(34):6238-6245.
180. Zhang H, Liao Q, Wu Y, et al. 2D Ruddlesden-Popper perovskites microring laser array. *Adv Mater.* 2018;30(15):e1706186.
181. Amgar D, Stern A, Rotem D, Porath D, Etgar L. Tunable length and optical properties of $CsPbX_3$ (X = cl, Br, I) nanowires with a few unit cells. *Nano Lett.* 2017;17(2):1007-1013.
182. Eaton SW, Fu A, Wong AB, Ning C-Z, Yang P. Semiconductor nanowire lasers. *Nat Rev Mater.* 2016;1(6):16028.
183. Yan R, Gargas D, Yang P. Nanowire photonics. *Nat Photonics.* 2009;3(10):569-576.
184. Fu Y, Meng F, Rowley MB, et al. Solution growth of single crystal methylammonium lead halide perovskite nanostructures for optoelectronic and photovoltaic applications. *J Am Chem Soc.* 2015;137(17):5810-5818.
185. Zhu H, Fu Y, Meng F, et al. Lead halide perovskite nanowire lasers with low lasing thresholds and high quality factors. *Nat Mater.* 2015;14(6):636-642.
186. Fu Y, Zhu H, Schrader AW, et al. Nanowire lasers of formamidinium lead halide perovskites and their stabilized alloys with improved stability. *Nano Lett.* 2016;16(2):1000-1008.
187. Eaton SW, Lai M, Gibson NA, et al. Lasing in robust cesium lead halide perovskite nanowires. *Proc Natl Acad Sci U S A.* 2016;113(8):1993-1998.
188. Petrov AA, Pellet N, Seo J-Y, et al. New insight into the formation of hybrid perovskite nanowires via structure directing adducts. *Chem Mater.* 2016;29(2):587-594.
189. Gu J, Wu J, Jin C, et al. Solvent engineering for high conversion yields of layered raw materials into large-scale freestanding hybrid perovskite nanowires. *Nanoscale.* 2018;10(37):17722-17729.
190. Zhang D, Eaton SW, Yu Y, Dou L, Yang P. Solution-phase synthesis of cesium lead halide perovskite nanowires. *J Am Chem Soc.* 2015;137(29):9230-9233.
191. Zhang D, Yu Y, Bekenstein Y, Wong AB, Alivisatos AP, Yang P. Ultrathin colloidal cesium Lead halide perovskite nanowires. *J Am Chem Soc.* 2016;138(40):13155-13158.
192. Zhang D, Yang Y, Bekenstein Y, et al. Synthesis of composition tunable and highly luminescent cesium lead halide nanowires through anion-exchange reactions. *J Am Chem Soc.* 2016;138(23):7236-7239.
193. He X, Liu P, Wu S, Liao Q, Yao J, Fu H. Multi-color perovskite nanowire lasers through kinetically controlled solution growth followed by gas-phase halide exchange. *J Mater Chem C.* 2017;5(48):12707-12713.
194. Tong Y, Bohn BJ, Bladt E, et al. From precursor powders to $CsPbX_3$ perovskite nanowires: one-pot synthesis, growth mechanism, and oriented self-assembly. *Angew Chem Int Ed.* 2017;56(44):13887-13 892.
195. Hofmann S, Ducati C, Neill RJ, et al. Gold catalyzed growth of silicon nanowires by plasma enhanced chemical vapor deposition. *J Appl Phys.* 2003;94(9):6005-6012.
196. Kong YC, Yu DP, Zhang B, Fang W, Feng SQ. Ultraviolet-emitting ZnO nanowires synthesized by a physical vapor deposition approach. *Appl Phys Lett.* 2001;78(4):407-409.

197. Chang PC, Fan Z, Wang D, et al. ZnO nanowires synthesized by vapor trapping CVD method. *Chem Mater.* 2004;16(24):5133-5137.
198. Park K, Lee JW, Kim JD, et al. Light-matter interactions in cesium lead halide perovskite nanowire lasers. *J Phys Chem Lett.* 2016;7(18):3703-3710.
199. Zhu F, Men L, Guo Y, et al. Shape evolution and single particle luminescence of organometal halide perovskite nanocrystals. *ACS Nano.* 2015;9(3):2948-2959.
200. Imran M, Di Stasio F, Dang Z, et al. Colloidal synthesis of strongly fluorescent $CsPbBr_3$ nanowires with width tunable down to the quantum confinement regime. *Chem Mater.* 2016;28(18):6450-6454.
201. Zhou H, Yuan S, Wang X, et al. Vapor growth and tunable lasing of band gap engineered cesium lead halide perovskite micro/nanorods with triangular cross section. *ACS Nano.* 2016;11(2):1189-1195.
202. Ashley MJ, O'Brien MN, Hedderick KR, Mason JA, Ross MB, Mirkin CA. Templated synthesis of uniform perovskite nanowire arrays. *J Am Chem Soc.* 2016;138(32):10096-10099.
203. Waleed A, Tavakoli MM, Gu L, et al. All inorganic cesium lead iodide perovskite nanowires with stabilized cubic phase at room temperature and nanowire array-based photodetectors. *Nano Lett.* 2017;17(8):4951-4957.
204. Oener SZ, Khoram P, Brittman S, et al. Perovskite nanowire extrusion. *Nano Lett.* 2017;17(11):6557-6563.
205. Waleed A, Tavakoli MM, Gu L, et al. Lead-free perovskite nanowire array photodetectors with drastically improved stability in nanoengineering templates. *Nano Lett.* 2017;17(1):523-530.
206. Wang X, Shoaib M, Wang X, et al. High-quality in-plane aligned $CsPbX_3$ perovskite nanowire lasers with composition-dependent strong exciton-photon coupling. *ACS Nano.* 2018;12(6):6170-6178.
207. Deng H, Yang X, Dong D, et al. Flexible and semitransparent organolead triiodide perovskite network photodetector arrays with high stability. *Nano Lett.* 2015;15(12):7963-7969.
208. Spina M, Bonvin E, Sienkiewicz A, Nafradi B, Forro L, Horvath E. Controlled growth of $CH_3NH_3PbI_3$ nanowires in arrays of open nanofluidic channels. *Sci Rep.* 2016;6:19834.
209. Hu Q, Wu H, Sun J, Yan D, Gao Y, Yang J. Large-area perovskite nanowire arrays fabricated by large-scale roll-to-roll micro-gravure printing and doctor blading. *Nanoscale.* 2016;8(9):5350-5357.
210. Zhuo S, Zhang J, Shi Y, Huang Y, Zhang B. Self-template-directed synthesis of porous perovskite nanowires at room temperature for high-performance visible-light photodetectors. *Angew Chem Int Ed.* 2015;127(19):5785-5788.
211. Yang T, Zheng Y, Du Z, et al. Superior photodetectors based on all-inorganic perovskite $CsPbI_3$ nanorods with ultrafast response and high stability. *ACS Nano.* 2018;12(2):1611-1617.
212. Dong D, Deng H, Hu C, et al. Bandgap tunable $Cs_x(CH_3NH_3)_{1-x}PbI_3$ perovskite nanowires by aqueous solution synthesis for optoelectronic devices. *Nanoscale.* 2017;9(4):1567-1574.
213. Jin W, Gao Z, Zhou Y, et al. Novel graphene-oxide-semiconductor nanowire phototransistors. *J Mater Chem C.* 2014;2(9):1592.
214. Zhang W, Chuu CP, Huang JK, et al. Ultrahigh-gain photodetectors based on atomically thin graphene-MoS_2 heterostructures. *Sci Rep.* 2014;4:3826.
215. Lopez-Sanchez O, Lembke D, Kayci M, Radenovic A, Kis A. Ultrasensitive photodetectors based on monolayer MoS_2. *Nat Nanotechnol.* 2013;8(7):497-501.
216. Konstantatos G, Badioli M, Gaudreau L, et al. Hybrid graphene-quantum dot phototransistors with ultrahigh gain. *Nat Nanotechnol.* 2012;7(6):363-368.
217. Schmidt LC, Pertegas A, Gonzalez-Carrero S, et al. Nontemplate synthesis of $CH_3NH_3PbBr_3$ perovskite nanoparticles. *J Am Chem Soc.* 2014;136(3):850-853.
218. Zhang F, Zhong H, Chen C, et al. Brightly luminescent and color-tunable colloidal $CH_3NH_3PbX_3$ (X = Br, I, cl) quantum dots: potential alternatives for display technology. *ACS Nano.* 2015;9(4):4533-4542.
219. Wei S, Yang Y, Kang X, Wang L, Huang L, Pan D. Room-temperature and gram-scale synthesis of $CsPbX_3$ (X = Cl, Br, I) perovskite nanocrystals with 50-85% photoluminescence quantum yields. *Chem Commun.* 2016;52(45):7265-7268.
220. Protesescu L, Yakunin S, Bodnarchuk MI, et al. Nanocrystals of cesium lead halide perovskites ($CsPbX_3$, X = Cl, Br, and I): novel optoelectronic materials showing bright emission with wide color gamut. *Nano Lett.* 2015;15(6):3692-3696.
221. Nedelcu G, Protesescu L, Yakunin S, Bodnarchuk MI, Grotevent MJ, Kovalenko MV. Fast anion-exchange in highly luminescent nanocrystals of cesium lead halide perovskites ($CsPbX_3$, X = Cl, Br, I). *Nano Lett.* 2015;15(8):5635-5640.
222. Parobek D, Dong Y, Qiao T, Son DH. Direct hot-injection synthesis of Mn-doped $CsPbBr_3$ nanocrystals. *Chem Mater.* 2018;30(9):2939-2944.
223. Yarema M, Yarema O, Lin WMM, et al. Upscaling colloidal nanocrystal hot-injection syntheses via reactor underpressure. *Chem Mater.* 2017;29(2):796-803.
224. Kojima A, Ikegami M, Teshima K, Miyasaka T. Highly luminescent lead bromide perovskite nanoparticles synthesized with porous alumina media. *Chem Lett.* 2012;41(4):397-399.
225. Malgras V, Tominaka S, Ryan JW, et al. Observation of quantum confinement in monodisperse methylammonium lead halide perovskite nanocrystals embedded in mesoporous silica. *J Am Chem Soc.* 2016;138(42):13874-13881.
226. Dirin DN, Protesescu L, Trummer D, et al. Harnessing defect-tolerance at the nanoscale: highly luminescent lead halide perovskite nanocrystals in mesoporous silica matrixes. *Nano Lett.* 2016;16(9):5866-5874.
227. Longo G, Pertegás A, Martínez-Sarti L, Sessolo M, Bolink HJ. Highly luminescent perovskite-aluminum oxide composites. *J Mater Chem C.* 2015;3(43):11286-11289.
228. Li X, Wu Y, Zhang S, et al. $CsPbX_3$ quantum dots for lighting and displays: room-temperature synthesis, photoluminescence superiorities, underlying origins and white light-emitting diodes. *Adv Funct Mater.* 2016;26(15):2435-2445.
229. Li X, Zhao Y-B, Fan F, et al. Bright colloidal quantum dot light-emitting diodes enabled by efficient chlorination. *Nat Photonics.* 2018;12(3):159-164.
230. Zhou C, Lin H, Tian Y, et al. Luminescent zero-dimensional organic metal halide hybrids with near-unity quantum efficiency. *Chem Sci.* 2018;9(3):586-593.
231. Cui BB, Han Y, Huang B, et al. Locally collective hydrogen bonding isolates lead octahedra for white emission improvement. *Nat Commun.* 2019;10(1):1-8.

232. Worku M, Tian Y, Zhou C, et al. Sunlike white-light-emitting diodes based on zero-dimensional organic metal halide hybrids. *ACS Appl Mater Interface*. 2018;10(36):30051-30057.
233. Cortecchia D, Yin J, Petrozza A, Soci C. White light emission in low-dimensional perovskites. *J Mater Chem C*. 2019;7(17):4956-4969.
234. Yakunin S, Protesescu L, Krieg F, et al. Low-threshold amplified spontaneous emission and lasing from colloidal nanocrystals of caesium lead halide perovskites. *Nat Commun*. 2015;6:8056.
235. Wang Y, Li X, Song J, Xiao L, Zeng H, Sun H. All-inorganic colloidal perovskite quantum dots: a new class of lasing materials with favorable characteristics. *Adv Mater*. 2015;27(44):7101-7108.
236. Wang Y, Li X, Zhao X, Xiao L, Zeng H, Sun H. Nonlinear absorption and low-threshold multiphoton pumped stimulated emission from all-inorganic perovskite nanocrystals. *Nano Lett*. 2016;16(1):448-453.
237. Pilania G, Mannodi-Kanakkithodi A, Uberuaga BP, Ramprasad R, Gubernatis JE, Lookman T. Machine learning bandgaps of double perovskites. *Sci Rep*. 2016;6:19375.
238. Pilania G, Balachandran PV, Kim C, Lookman T. Finding new perovskite halides via machine learning. *Front Mater*. 2016;3(19):1-7.
239. Lu S, Zhou Q, Ouyang Y, Guo Y, Li Q, Wang J. Accelerated discovery of stable lead-free hybrid organic-inorganic perovskites via machine learning. *Nat Commun*. 2018;9(1):3405.
240. De Luna P, Wei J, Bengio Y, et al. Use machine learning to find energy materials. *Nature*. 2017;552(7683):23-27.
241. Kim C, Pilania G, Ramprasad R. Machine learning assisted predictions of intrinsic dielectric breakdown strength of ABX_3 perovskites. *J Phys Chem C*. 2016;120(27):14575-14580.
242. He Y, Galli G. Perovskites for solar thermoelectric applications: a first principle study of $CH_3NH_3AI_3$(A = Pb and Sn). *Chem Mater*. 2014;26(18):5394-5400.
243. Mettan X, Pisoni R, Matus P, et al. Tuning of the thermoelectric figure of merit of $CH_3NH_3MI_3$ (M = Pb,Sn) photovoltaic perovskites. *J Phys Chem C*. 2015;119(21):11506-11510.
244. Wang Y, Lin R, Zhu P, et al. Cation dynamics governed thermal properties of Lead halide perovskite nanowires. *Nano Lett*. 2018;18(5):2772-2779.
245. Kong Q, Lee W, Lai M, et al. Phase-transition-induced p-n junction in single halide perovskite nanowire. *Proc Natl Acad Sci U S A*. 2018;115(36):8889-8894.
246. Lee W, Li H, Wong AB, et al. Ultralow thermal conductivity in all-inorganic halide perovskites. *Proc Natl Acad Sci U S A*. 2017;114(33):8693-8697.
247. Wang Y, Zhang Y, Pang T, et al. Organolead halide perovskite-based metal-oxide-semiconductor structure photodetectors achieving ultrahigh detectivity. *Sol Energy*. 2019;183:226-233.
248. Luan S-Z, Wang Y-C, Liu Y-T, Jia R-X. Effect of depositing PCBM on perovskite-based metal-oxide-semiconductor field effect transistors. *Chin Phys B*. 2018;27(4):047208.
249. Liao WQ, Zhang Y. Hu C L, et al. A lead-halide perovskite molecular ferroelectric semiconductor. *Nat Commun*. 2015;6:7338.

AUTHOR BIOGRAPHIES

Pengchen Zhu is currently a PhD student in the College of Engineering and Applied Sciences at Nanjing University. His research mainly focuses on metal halide perovskite solar cells.

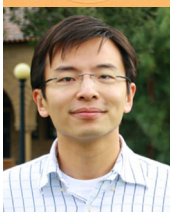

Jia Zhu is a professor in the College of Engineering and Applied Sciences at Nanjing University. He received his PhD degree in Electrical Engineering from Stanford University in 2010. He worked as a postdoctoral scholar at the University of California, Berkeley. He now leads a group of researchers working on nanomaterials for energy conversion and storage.

How to cite this article: Zhu P, Zhu J. Low-dimensional metal halide perovskites and related optoelectronic applications. *InfoMat*. 2020;1–38. https://doi.org/10.1002/inf2.12086